Missing Link: Bayesian detection and measurement of intermediate-mass black-hole binaries

Philip B. Graff,[1,2,3,*] Alessandra Buonanno,[4,1] and B. S. Sathyaprakash[5,4]

[1]*Department of Physics, University of Maryland, College Park, Maryland 20742, USA*
[2]*Gravitational Astrophysics Laboratory, NASA Goddard Space Flight Center,*
8800 Greenbelt Road, Greenbelt, Maryland 20771, USA
[3]*Joint Space-Science Institute, University of Maryland, College Park, Maryland 20742, USA*
[4]*Max Planck Institute for Gravitational Physics (Albert Einstein Institute),*
Am Mühlenberg 1, Potsdam-Golm 14476, Germany
[5]*School of Physics and Astronomy, Cardiff University, Queens Building,*
CF24 3AA Cardiff, United Kingdom

We perform Bayesian analysis of gravitational-wave signals from nonspinning, intermediate-mass black-hole binaries (IMBHBs) with observed total mass, M_{obs}, from $50 M_\odot$ to $500 M_\odot$ and mass ratio 1–4 using advanced LIGO and Virgo detectors. We employ inspiral-merger-ringdown waveform models based on the effective-one-body formalism and include subleading modes of radiation beyond the leading (2,2) mode. The presence of subleading modes increases signal power for inclined binaries and allows for improved accuracy and precision in measurements of the masses as well as breaking of degeneracies in distance, orientation and polarization. For low total masses, $M_{obs} \lesssim 50 M_\odot$, for which the inspiral signal dominates, the observed chirp mass $\mathcal{M}_{obs} = M_{obs} \eta^{3/5}$ (η being the symmetric mass ratio) is better measured. In contrast, as increasing power comes from merger and ringdown, we find that the total mass M_{obs} has better relative precision than $\mathcal{M}_{obs}$. Indeed, at high M_{obs} ($\geq 300 M_\odot$), the signal resembles a burst and the measurement thus extracts the dominant frequency of the signal that depends on M_{obs}. Depending on the binary's inclination, at signal-to-noise ratio (SNR) of 12, uncertainties in M_{obs} can be as large as ~ 20–25% while uncertainties in $\mathcal{M}_{obs}$ are ~ 50–60% in binaries with unequal masses (those numbers become $\sim 17\%$ vs. $\sim 22\%$ in more symmetric mass-ratio binaries). Although large, those uncertainties in M_{obs} will establish the existence of IMBHs. We find that effective-one-body waveforms with subleading modes are essential to confirm a signal's presence in the data, with calculated Bayesian evidences yielding a false alarm probability below 10^{-5} for SNR $\gtrsim 9$ in Gaussian noise. Our results show that gravitational-wave observations can offer a unique tool to observe and understand the formation, evolution and demographics of IMBHs, which are difficult to observe in the electromagnetic window.

I. INTRODUCTION

Advanced interferometric gravitational-wave (GW) detectors LIGO and Virgo will be turned on in late 2015 (2016 for Virgo) and are expected to reach design sensitivity by 2019 [1–4]. At design sensitivity these detectors will operate in the frequency range from 10 Hz to 1 kHz, with an almost flat sensitivity from 40 Hz to 1 kHz. In Fig. 1, we show for the advanced LIGO-Virgo network, the distance reach[1] as a function of observed total mass for the full inspiral-merger-ringdown signal of binaries consisting of nonspinning black holes (BHs) and include several multipole modes beyond the dominant ($\ell = 2, m = 2$)

mode, as well as higher order post-Newtonian (PN) corrections (see Sec. II for details) [5]. For nonspinning binary black holes (BBHs) with mass-ratio 1 (mass-ratio 4) of observed total mass $\sim 200 M_\odot$ and $\sim 800 M_\odot$, the distance reach is ~ 5 Gpc (respectively, ~ 3 Gpc), with the largest reach of ~ 6.5 Gpc (respectively, ~ 4 Gpc) for $\sim 400 M_\odot$ (see Fig. 1). The intrinsic mass (i.e., the rest-frame mass) of a binary M is related to the observed mass M_{obs} by $M_{obs} = (1 + z)M$, and so the intrinsic masses detected at these redshifts are significantly smaller than the observed masses. As we see from Fig. 1, subleading modes become increasingly important close to coalescence and their impact on the SNR is relevant for BBHs of total mass $\gtrsim 200 M_\odot$, especially for asymmetric binaries whose orbital plane is inclined with respect to the line-of-sight.

The increase in the distance reach brought about by the use of subleading modes is greater for these latter systems as compared to face-on, equal-mass systems where the increase is negligible. When spins are included, the

---

[*]pgraff@umd.edu
[1]For a network consisting of two advanced LIGO and Virgo detectors, we compute the distance reach as the root-mean-square distance, averaged over the whole sky and polarization angle, at which the network SNR is equal to 12. We do not average over the inclination angle, but instead we use a typical value of $\pi/3$.
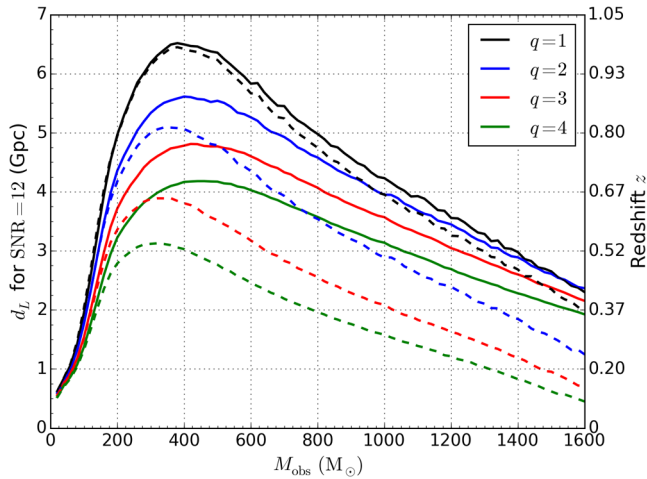
FIG. 1 (color online). We show the distance reach as a function of the observed total mass M_{obs} for several values of the binary mass ratio q. The reach is computed using a detector network consisting of two advanced LIGO interferometers and advanced Virgo, using a network SNR = 12. Detector sensitivities are given by the advanced LIGO and Virgo design curves [6]; the advanced LIGO design is the zero-detuned high-power (ZDHP) noise curve. The right y-axis shows the redshift computed assuming cosmological parameters measured by the Planck satellite [7]. The continuous curves use inspiral-merger-ringdown waveforms with the most dominant five modes (EOBNRv2HM), while the dashed curve only includes the (2,2) mode (EOBNRv2). The values here are numerically averaged over sky location and polarization, with fixed orbital phase and inclination: $\{\phi, \theta_{\mathrm{JN}}\} = \{0, \pi/3\}$ rad. The coalescence time is also fixed to a GPS time of $t_c = 1000000008$ s, corresponding to Sept. 14, 2011 01:46:33 UTC.

distance reach can be a factor of two larger (for near maximal BH spins aligned with the orbital angular momentum) or smaller (for maximal spins antialigned with the orbital angular momentum) [8–10]. Thus, advanced LIGO and Virgo could detect BBHs in the hundred solar mass range with a SNR = 12 up to $z \sim 2$, depending on the mass ratio of the system and spin.

The above mass range falls in the domain of so-called *intermediate mass* black holes (IMBHs). The formation mechanism, evolutionary history and mass function of IMBHs are largely unknown, as it is very difficult to observe them and measure their masses in the electromagnetic window. Several mechanisms have been proposed for their birth and evolution [10–13]. There is now substantial evidence that galactic nuclei contain massive BHs of millions to billions of solar masses but they are believed to have been seeded by lighter BHs of hundreds or thousands of solar masses (for a review, see, e.g. Refs. [12,14]). While there is also firm support for the existence of stellar mass BH candidates [15], the IMBH population seems to be missing and there is only indirect evidence of their existence. For example, it is suspected that IMBHs could be responsible for ultraluminous X-ray sources. While not all such sources are

believed to host an IMBH [16], some of them do show evidence of BHs of tens to hundreds of solar masses. These include a stellar mass BH of $<15\mathrm{M}_\odot$ in NGC7793 [17], a more massive $20\mathrm{M}_\odot$–$30\mathrm{M}_\odot$ BH in M101 ULX-1 [18] and a $\sim 400\mathrm{M}_\odot$ IMBH in M82 [19].

At present we do not know of any IMBH binaries (IMBHB). However, astrophysical scenarios of their formation have been proposed in the literature, which include hierarchical growth of black holes at galactic nuclei by accretion of gas, stars and compact objects (i.e. neutron stars and black holes) and dynamical capture of smaller black holes by nuclear black holes in stellar clusters. Hierarchical models of structure formation predict that supermassive BHs found in galactic nuclei might initially be IMBHs that grow to their current size by accreting gas and merging with other IMBHs [11,12,14,20–22]. In such a scenario we might expect mergers of IMBHBs when the Universe began assembling the large structure at high redshift ($z \sim 10$–20). Such mergers might have continued in the local Universe, but it is very difficult to compute merger rates as we do not fully understand the initial conditions for IMBHs (mass function of seed BHs and their spins), their binaries (orbital parameters at formation and population as a function of mass ratio), or the process by which they grow (accretion of gas and merger with other BHs).

Besides growing their mass by dynamical capture in stellar clusters, massive BHs may form from the collapse of massive stars and until recently both observations and theoretical arguments suggested that stars above $150\mathrm{M}_\odot$ do not form at nonzero metallicity. However, recent observations of several stars with current masses larger than $150\mathrm{M}_\odot$ in the R136 region of the Large Magellanic Cloud triggered a reanalysis [10] of the possibility that very massive BHs can have stellar origin. Reference [10] found that very massive stellar-origin BHs with mass larger than $100\mathrm{M}_\odot$ can form only in low-metallicity environments (i.e., $Z \leq 0.1$–$0.4Z_\odot$), if the initial mass function extends above $500\mathrm{M}_\odot$ and pair-instability supernovae do not destroy stars with mass above $500\mathrm{M}_\odot$. Moreover, the formation of close massive BH binaries requires that the very massive stars above $500\mathrm{M}_\odot$ expand by a factor of 2 and go through and survive a common envelope phase. If these requirements are met, then massive BH binaries are expected to have mass ratios of at most a few, spins primarily aligned with the orbital angular momentum, and negligible eccentricity when they enter the advanced LIGO band [23]. If the above requirements are not met, then they will have too wide a separation to coalesce within a Hubble time. However, other phenomena in dense stellar environments (e.g., cluster binary-single interactions) and in low-density field populations (e.g, Kozai mechanism in triple systems) can lower the coalescence time of wide massive BH binaries. The investigation carried out in Ref. [10] concluded that on the order of a few massive BH binaries of stellar-origin could be observed by

advanced LIGO and Virgo. However, due to astrophysical and theoretical uncertainties, the number of detections per year can be as high as hundreds or as low as zero.

In this paper we use state-of-the-art waveform models to explore how well advanced GW detectors can measure the physical parameters of an IMBHB. Signals from IMBHB coalescences have several important features that should be incorporated in a study of how GW observations will help to measure the parameters of such systems. First, as several previous studies have already pointed out (see, e.g., Ref. [24] and references therein), in advanced GW detectors, the plunge, merger and quasinormal-mode ringdown phases of evolution contribute significantly to the detectors' distance reach if the binary has a total mass larger than about $\sim 50 M_\odot$. This means that we must use the *full* signal, that is not only the adiabatic inspiral phase, but also the merger and ringdown portions. Second, binaries formed in the field will most likely have negligible eccentricity [25] as they enter the sensitivity band of advanced detectors and can be assumed to trace quasicircular orbits. For binaries undergoing dynamical capture or Kozai mechanism in star clusters, advanced LIGO and Virgo might detect mild eccentricities [26], if $M_{\rm obs} \sim 10$–$20 M_\odot$. For massive BHs, we expect negligible eccentricities when the binary enters the detector band. Indeed, for a fixed mass ratio and speed at infinity, the pericenter distance at capture is proportional to the total mass [23]. Thus, the frequency at capture is inversely proportional to the total mass. As a result, larger total masses result in lower capture frequencies and thus circularize more by the time the binary gets to a fixed frequency, such as 10 Hz.

In this study we assume our systems to have zero eccentricity. Thus the gravitational wave emission in *comparable mass* binaries will be dominated by the ($\ell = 2$, $m = 2$) mode at twice the orbital frequency, at least until merger. Asymmetric systems with unequal masses, nevertheless, emit radiation at other multiples of the orbital frequency or subleading modes (see, e.g., Sec. 10.4 in Ref. [27]). As shown by several authors [28–35] these subdominant modes can be important in the inspiral phase in improving the accuracy with which parameters are deduced from GW observations, especially when the mass ratio of the binary is large. The amplitude of those subleading modes grows more and more toward merger [5,36–38]. As a consequence, relevant properties of the progenitor binary can be recovered from the relative amplitudes of the subleading modes excited in the BH remnant [39–44] and tests of general relativity [45,46] can be carried out when those subdominat modes are included during merger and ringdown. Moreover, for the purposes of signal candidate detection in template bank searches, Ref. [47] showed that when constructing banks for BBH searches, the inclusion of subdominant modes yielded improved sensitivity for systems with $M_{\rm obs} \gtrsim 100 M_\odot$ and $q \gtrsim 4$ (where $q \equiv m_1/m_2 \geq 1$ is the mass

ratio). Third, waveforms from nonspinning BH binaries on quasicircular orbits are very simple chirplike signals, with monotonically increasing frequency and amplitude. However, BH spins can cause amplitude and phase modulations, so one must ideally include spin effects in the waveform model, unless the IMBH formation scenario strongly suggests nonprecessing or negligible spins [10], if the BHs grow their mass through multiple mergers in stellar clusters. In this paper, however, we will limit ourselves to nonspinning BH binaries as waveforms that include both spin effects and subleading modes are not yet available.

The rest of the paper is organized as follows. In Sec. II we describe the inspiral, merger and ringdown template family used in our analysis, its parameters and the main features introduced by the subdominant modes. In Sec. III we review the basics of Bayesian inference, the sampling technique that we use (i.e., nested sampling) and the priors employed in our study. In Sec. IV we discuss how the Bayesian evidence of the GW signal can be used to confirm detection, how the false alarm probability can be obtained from the Bayesian evidence, and how the Bayesian evidence changes depending on the inclusion of the subdominant modes. In Sec. V we discuss how Bayesian parameter measurement depends on the binary's total mass, mass ratio, inclusion of subleading modes and priors, and compare our study to previous ones. We also discuss the astrophysical implications of these measurements of IMBHBs. Finally, in Sec. VI we draw our main conclusions.

II. WAVEFORMS

In this section we will discuss the waveform family used in this study and the parameters used to describe the signal as observed by a detector. In particular, we discuss the importance of the subleading modes and the merger and ringdown phases of the signal for IMBHBs. We demonstrate this by first plotting the signal as observed by an advanced detector and discuss how the SNR is accumulated as a function of time. We will also plot the signal power spectrum and highlight the relevance of subleading modes for unequal-mass systems whose orbital plane is inclined with respect to the line-of-sight.

A. Inspiral-merger-ringdown waveforms and parameters

In this study we employ nonspinning waveforms constructed within the effective-one-body (EOB) formalism [48,49] and calibrated to highly-accurate numerical relativity (NR) simulations having typical length of 30–40 GW cycles and mass ratios $q \leq 6$ [5]. More specifically, we use the EOBNRV2HM code in the LIGO Algorithm Library (LAL) [50] to generate the EOB waveform model in Ref. [5], which includes four subleading modes, namely the $(l, m) = (2, 1), (3,3), (4,4)$ and $(5,5)$ modes, as well as

the leading $(l, m) = (2, 2)$ mode.[2] [These modes come from the decomposition of the GW signal $h = h_+ - \imath h_\times$ into -2 spin-weighted spherical harmonics $_{-2}Y_{lm}$ [5].] Consequently, GW signals that we study contain the first five harmonics of the orbital frequency. During most of the early inspiral phase only the (2,2) mode, and, in particular, its Newtonian amplitude, will be the dominant component. Other harmonics and PN corrections become increasingly important as we get close to merger. The effect of these higher modes is especially relevant when the binary in question has its merger and ringdown frequencies in the most sensitive part of a detector's response. The ringdown frequency of the final remnant of binaries consisting of nonspinning BHs of total mass $50 M_\odot$ to $500 M_\odot$ varies over the range 40 Hz to 400 Hz—the frequency range where LIGO and Virgo have the best sensitivity, and this provides the motivation for our choice of masses used in this study.

A Markov-chain Monte-Carlo (MCMC) study [32] demonstrated that the EOB waveforms of Ref. [5] are indistinguishable from the NR waveforms [52] used to calibrate them up to SNR = 50 for advanced LIGO detectors. Subsequent investigations carried out in Ref. [53] verified the accuracy of these nonspinning EOB waveforms in the entire sensitivity band of advanced LIGO detectors and suggested that the EOB model be accurate even outside the region of calibration, i.e. when $q > 6$. This expectation was verified by the very good agreement found against the $q = 10$ NR waveform of 20 GW cycles in Ref. [54] and, especially, against the $q = 7$ NR waveform of 350 GW cycles recently produced by the SXS collaboration [55].

Since in our study we consider BBHs in quasicircular orbits with negligible spins, the system can be described by nine parameters: $\boldsymbol{\theta} = \{m_1, m_2, d_L, t_c, \delta, \alpha, \theta_{JN}, \psi, \phi\}$. The parameters m_1 and m_2 are the masses of the individual BHs. From these quantities we define the total intrinsic mass, $M = (m_1 + m_2)$, the total observed mass, $M_{obs} = M(1 + z)$ with z being the redshift, the mass ratio, $q = m_1/m_2 \geq 1$, the symmetric mass ratio, $\eta = m_1 m_2/(m_1 + m_2)^2 = q/(1 + q)^2$, the intrinsic chirp mass, $\mathcal{M} = M\eta^{3/5}$ and the observed chirp mass, $\mathcal{M}_{obs} = \mathcal{M}(1 + z)$. The parameter d_L is the luminosity distance and when combined with the declination δ and right ascension α, it defines the sky location of the binary. The time of the peak in the (2,2) mode of the waveform, as measured at the geocenter, is given by t_c; this serves as an approximation of the merger time. The angle θ_{JN} measures the inclination of the binary's total angular momentum $\mathbf{J}$ (equal to the orbital angular momentum, $\mathbf{L}$, as the holes are nonspinning) with respect to the line of sight from the detectors $\mathbf{n}$ (geocenter). The

polarization ψ and the phase ϕ provide the additional Euler angles necessary to describe the rotation from $\mathbf{n}$ to $\mathbf{J}$.

B. Accumulation of SNR in waveforms

In this paper we are interested in studying the effect on parameter estimation of binary systems with larger and larger total masses. When we maintain a constant SNR and increase the binary's total mass, the signal moves downward in frequency space, resulting in more power from the merger and ringdown portions as opposed to the inspiral. The merger occurs at approximately the frequency of the last stable orbit (LSO), which in the case of a Schwarzschild BH is $f_{LSO} \simeq 4400(M_\odot/M)$ Hz. We begin our integration at $f_{min} = 10$ Hz, so for systems with $M_{obs} \geq 400 M_\odot$ there will be little power from the inspiral portion of the waveform. As the inspiral evolution is dominated by $\mathcal{M}_{obs}$ and the merger and ringdown are dominated by M_{obs}, we expect the character of the parameter estimation to transition from one to the other (see Sec. V).

To demonstrate this expectation, we compare in Fig. 2 two waveforms with $M_{obs} = 50 M_\odot$ and $400 M_\odot$. We show both the original waveform and the waveform normalized by the advanced LIGO zero-detuned high-power (ZDHP) power spectral density (PSD), $S_n(f)$; the normalized waveform has been rescaled so that it has the same amplitude at $t = 0$ as the original. The comparisons clearly show that for the $(M_{obs}, q) = (50 M_\odot, 1)$ waveform, 90% of the power (SNR^2) has been accumulated during the inspiral and that the merger and ringdown play only a minor role. On the other hand, for the $(M_{obs}, q) = (400 M_\odot, 1)$ waveform, only 10% of the power is collected during the inspiral and now the merger and ringdown are predominant features. In Fig. 3 we show the amplitudes of the waveforms in frequency space in comparison to the advanced LIGO ZDHP and advanced Virgo design $\sqrt{S_n(f)}$. We can see in Fig. 3 that for the higher-mass waveforms, the entire inspiral signal is strongly down-weighted by the rising of the amplitude spectral density with the merger occurring as $\sqrt{S_n(f)}$ reaches a minimum. For the lower-mass waveforms, much of the inspiral is in the frequency band where the amplitude spectral density is at or near minimum, thereby allowing this part of the waveform to dominate.

III. BAYESIAN INFERENCE

This section will provide a short background to Bayesian inference. We will focus on the application of Bayesian analysis to the problems of detection, parameter estimation and model selection that will be used in Secs. IV and V in the context of GW observations of IMBHBs. After a brief introduction to the basics of Bayesian methods, we will discuss a specific technique called *nested sampling* that is used to efficiently compute Bayesian *evidence*, followed by

---

[2]An EOB model with different parametrization was subsequently calibrated to the same set of NR waveforms used in Ref. [5] and provides two subleading modes $(l, m) = (2, 1)$ and $(3, 3)$ [51], besides the leading one.
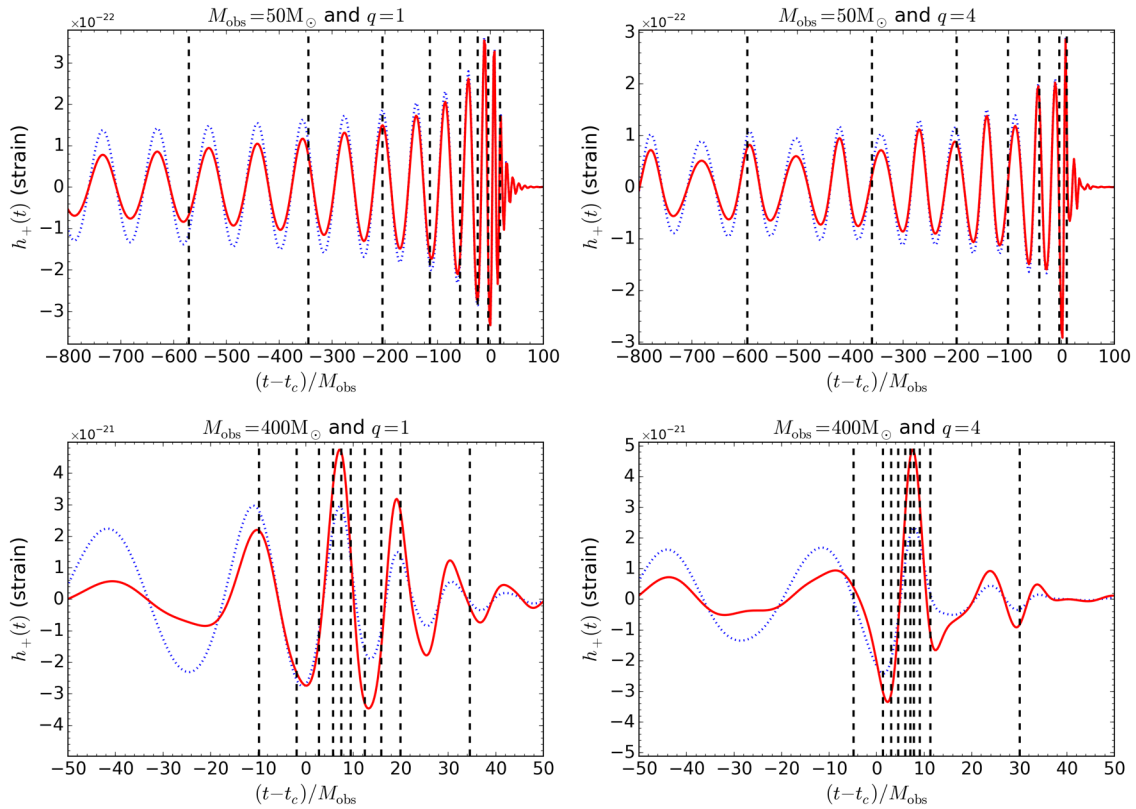
FIG. 2 (color online).   We display EOBNR waveforms with subleading modes used in this study. We plot the plus polarization of each waveform: original (dotted blue), and normalized by the PSD (and then scaled to have equal amplitude at $t = 0$ as original) (solid red). The plots in the top row have $M_{obs} = 50 M_{\odot}$ and in the bottom row have $M_{obs} = 400 M_{\odot}$; the left column has $q = 1$ and the right column has $q = 4$. The time axis is scaled by the observed total mass of the system. Vertical lines are at intervals of 10% of signal power with the right most line at 99%. All systems are observed at an inclination of $\theta_{JN} = \pi/3$ rad and a distance of $d_L = 1$ Gpc.
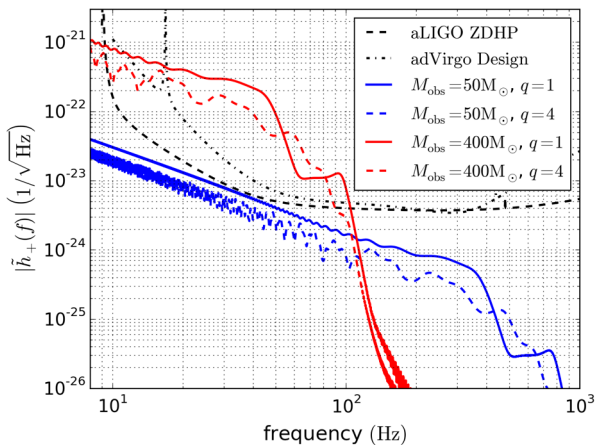

FIG. 3 (color online).   We show the Fourier-domain amplitudes of the waveforms displayed in Fig. 2. Extra structure from subdominant modes can be clearly seen in the nonequal mass cases. For comparison, we also display the advanced LIGO ZDHP and advanced Virgo design amplitude spectral density $\sqrt{S_n(f)}$. For all waveforms we use $d_L = 1$ Gpc and $\theta_{JN} = \pi/3$ rad.

a description of our choice of prior probabilities for various parameters and how we compute the *likelihood* function.

A. Basics of Bayesian methods

Bayesian inference provides a statistically rigorous method of measuring the probability distribution of a set of parameters $\boldsymbol{\theta}$ given a model or hypothesis $\mathcal{H}$ and a set of data $\mathcal{D}$. Bayes' theorem states that

$$\Pr(\boldsymbol{\theta}|\mathcal{D}, \mathcal{H}) = \frac{\Pr(\mathcal{D}|\boldsymbol{\theta}, \mathcal{H}) \Pr(\boldsymbol{\theta}|\mathcal{H})}{\Pr(\mathcal{D}|\mathcal{H})}, \qquad (1)$$

where $\Pr(\boldsymbol{\theta}|\mathcal{D}, \mathcal{H})$ is the posterior probability distribution of parameters used for making inferences about which signal parameters $\boldsymbol{\theta}$ best fit the data and what the corresponding credible regions are; $\Pr(\mathcal{D}|\boldsymbol{\theta}, \mathcal{H})$ is the likelihood of obtaining the data given the specific model and parameters, for which we use the shorthand $\mathcal{L}(\boldsymbol{\theta})$; $\Pr(\boldsymbol{\theta}|\mathcal{H})$ is the prior probability of the parameters for the model that represents our knowledge of these values before looking at the data (*a priori*); and $\Pr(\mathcal{D}|\mathcal{H})$ is the Bayesian evidence, which is commonly abbreviated as $\mathcal{Z}$.

The evidence is the factor needed to normalize the posterior distribution and can therefore also be expressed as

$$\mathcal{Z} = \int_{\Theta} \mathcal{L}(\boldsymbol{\theta}) \Pr(\boldsymbol{\theta}|\mathcal{H}) d^N \boldsymbol{\theta}, \tag{2}$$

where N is the dimensionality of the parameter space. Since $\mathcal{Z}$ is independent of the parameters, it can be safely ignored for parameter estimation problems, but it is still useful in model comparison.

When comparing two models, $\mathcal{H}_0$ and $\mathcal{H}_1$, one can write their relative probabilities as

$$\frac{\Pr(\mathcal{H}_1|\mathcal{D})}{\Pr(\mathcal{H}_0|\mathcal{D})} = \frac{\mathcal{Z}_1}{\mathcal{Z}_0} \frac{\Pr(\mathcal{H}_1)}{\Pr(\mathcal{H}_0)}, \tag{3}$$

where we used Bayes' theorem again and have canceled out $\Pr(\mathcal{D})$ and substituted in $\mathcal{Z}_i = \Pr(\mathcal{D}|\mathcal{H}_i)$ as appropriate. The relative probability of the two models is thus the ratio of their Bayesian evidences multiplied by the relative probability prior to considering the data. In our analysis, we will take the latter to be 1 and consider the ratio of the Bayesian evidences, which is called the odds ratio. In the problem of signal detection, $\mathcal{H}_0$ can be considered the noise-only model while $\mathcal{H}_1$ is the signal-plus-noise model. Therefore, an odds ratio much greater than 1 indicates a strong belief in the presence of a signal. This method naturally incorporates Occam's razor, such that more complicated models are penalized and must sufficiently improve the fit to the data to be favored.

B. Nested sampling and MULTINEST

Nested sampling [56] is a Bayesian inference technique developed for the calculation of the evidence, through which posterior probability samples are produced as a by-product. This is done by transforming the N-dimensional integral for $\mathcal{Z}$ into a 1-dimensional integral over the prior volume. We define the prior volume X by $dX = \Pr(\boldsymbol{\theta}|\mathcal{H}) d^N \boldsymbol{\theta}$. We can therefore write the prior probability volume enclosed within a contour (in parameter space) of constant likelihood λ as

$$X(\lambda) = \int_{\mathcal{L}(\boldsymbol{\theta}) > \lambda} \Pr(\boldsymbol{\theta}|\mathcal{H}) d^N \boldsymbol{\theta}. \tag{4}$$

The evidence integral of Eq. (2) can be rewritten as

$$\mathcal{Z} = \int_0^1 L(X) dX, \tag{5}$$

where $L(X)$ is the inverse of Eq. (4) (returns the likelihood at which a prior volume of X is enclosed) and is a monotonically decreasing function of X (i.e. more prior volume implies lower likelihood contour bound). If we can evaluate likelihood values $L_i = L(X_i)$ such that X_i is a

sequence of monotonically decreasing values, the evidence can be computed as a simple sum

$$\mathcal{Z} = \sum_{i=1}^M L_i w_i. \tag{6}$$

Here, the w_i are weights which can be taken from a simple trapezium rule such that $w_i = \frac{1}{2}(X_{i-1} - X_{i+1})$.

The individual prior weight of each sampled point can also be estimated from the sequence of X_i values. This may be combined with the computed likelihood for that point and the evidence to produce a final posterior probability for the point. The full sequence of points can then be resampled accordingly to the points' individual probabilities to produce a set of samples from the posterior.

Nested sampling operates by starting with an initial set of "live" points sampled from the prior distribution. Iterations are then performed whereby the point with lowest likelihood value is removed from the live point set and a new point is sampled from the prior with the restriction that it has higher likelihood than the point just removed. This removal and replacement is continued until a stopping condition is reached (e.g., a tolerance on the evidence calculation). The difficult task here lies in the efficient sampling of new points under this restriction. As the likelihood contour moves upward, the volume of the prior within that contour will decrease to very small values, making direct sampling of the prior very inefficient. The MULTINEST algorithm [57–59] addresses this by enclosing the live points in clusters of ellipsoids. A new sample can then be made from the ellipsoids very quickly and as they shrink along with the live points, they create effective likelihood contours to be sampled from, thereby greatly increasing the sampling efficiency. The ellipsoids can be distributed to enclose degenerate and multimodal distributions, making this approach very robust.

MULTINEST is implemented within BAMBI [60], which is linked with the LALINFERENCE [61] code of LAL. The `lalinference_bambi` sampler is used for analysis of simulated signals in this study.

C. Priors used

The priors used in this analysis are flat in the component masses, with $\{m_1, m_2\} \in [10, 600] M_\odot$ and $m_1 \geq m_2$. In Sec. V D, we assess the effect of changing the prior by implementing an alternative mass prior that is flat in the log of chirp mass for $\mathcal{M} \in [2.45, 435.275] M_\odot$ and flat over $\eta \in [0.03, 0.25]$.

In both setups, the source location prior is uniform in volume, thus proportional to d_L^2 for $d_L \in [100 \text{ Mpc}, 10 \text{ Gpc}]$ and flat in $\sin(\delta)$ and α for $\delta \in [0, \pi]$ rad and $\alpha \in [0, 2\pi]$ rad. We use a prior flat in coalescence time that is centered on the true value with $\Delta t_c \in [-0.1, 0.1]$ s. The orientation angles are assumed to be isotropically

distributed, thus flat in $\sin(\theta_{JN})$, ψ, and ϕ for $\theta_{JN} \in [0, \pi]$ rad, $\psi \in [0, \pi)$ rad, and $\phi \in [0, 2\pi)$ rad.

D. Likelihood function

In general, the data obtained from advanced LIGO and Virgo detectors is the sum of signal, **h**, and noise, **n**,

$$\mathbf{d} = \mathbf{h} + \mathbf{n}. \tag{7}$$

The signal in a given detector is given by

$$\mathbf{h} = \mathbf{F}_+(\alpha, \delta, \psi)\mathbf{h}_+ + \mathbf{F}_\times(\alpha, \delta, \psi)\mathbf{h}_\times, \tag{8}$$

where $\mathbf{h}_{+,\times}$ are the two independent GW polarizations and $\mathbf{F}_{+,\times}(\alpha, \delta, \psi)$ are the antenna response functions [62] that depend on the source location and polarization. The antenna response is slowly varying in time due to the rotation of the Earth, but this effect is small for the short duration of the signals considered in this study (<2 min).

The noise is modeled as independent and Gaussian in each frequency with a mean of zero and variance given by the detector's PSD. Therefore, the probability of a data stream, $\mathbf{d}_a$, in detector a containing a given signal, $\mathbf{h}(\boldsymbol{\theta})$, is given by the probability of the resulting noise realization, $\mathbf{n} = \mathbf{d} - \mathbf{h}(\boldsymbol{\theta})$. This is given by the product (sum in log-space) of the probability of the noise for each frequency bin [61]:

$$\begin{aligned}\log \mathcal{L}_a(\boldsymbol{\theta}) &= \log \Pr(\mathbf{d}_a | H_S, \boldsymbol{\theta}, S_n(f)) \\ &= -\frac{1}{2} \sum_i \left[\frac{4}{T} \frac{|\tilde{\mathbf{d}}_{a,i} - \tilde{\mathbf{h}}_i(\boldsymbol{\theta})|^2}{S_n(f_i)} + \log\left(\frac{\pi T S_n(f_i)}{2}\right) \right],\end{aligned} \tag{9}$$

where T is the segment length, the tilde indicates the discrete Fourier transform of the function, and i is an index over frequency bins. The noise power spectral density $S_n(f)$ will vary from detector to detector and here we use the ones at design sensitivity for advanced LIGO and Virgo [6].[3] H_s indicates that we are using the signal model that assumes a signal is present; this will be compared to the noise-only model, H_n, where $\mathbf{h} = \mathbf{0}$. The final likelihood is the product of likelihoods from the individual detectors,

$$\log \mathcal{L}(\boldsymbol{\theta}) = \sum_a \log \mathcal{L}_a(\boldsymbol{\theta}). \tag{10}$$

To simulate the sensitivity for advanced LIGO and Virgo detectors, we use a minimum frequency of $f_{\min} = 10$ Hz. In order to include the highest ringdown mode for the lowest possible total mass system, we use a sampling rate of 4096 Hz, giving a Nyquist frequency of $f_{\mathrm{Nyq}} = 2048$ Hz

---

[3]See https://dcc.ligo.org/LIGO-P1200087-v19/public for PSD data files

for the upper bound of our likelihood sum. A segment length of 128 s ensures that no waveforms are cut off in-band.

IV. BAYESIAN DETECTION

It is computationally infeasible to perform a Bayesian analysis over the entire detector data set, for all signal types, at all times. Therefore, alternative analysis pipelines are used to first produce candidate triggers for follow-up analyses using Bayesian inference over a small data set and parameter space [63,64]. In the search for BBHs, a discrete bank of template waveforms [65–67] is used to perform matched filter analysis of the data. The matches that cross a preset threshold are ranked by a reweighted SNR [63,64] and their significance is measured by comparison to the estimated background (i.e. noise-generated) triggers. This is a frequentist method of detection (and significance measurement) and is very useful for generating triggers which then receive a more detailed follow-up with Bayesian analysis and other tools. It is the first step in identifying and confirming a GW signal with LIGO and Virgo.

In Bayesian inference, one can make claims on the presence of a signal in data by means of model comparison. This is not the same as trigger/candidate finding, but rather looking at the evidence that the candidate is indeed a real GW signal. We compare the signal-plus-noise and noise-only models, H_s and H_n, and their respective evidences, $\mathcal{Z}_s$ and $\mathcal{Z}_n$. The probability that random noise would produce an evidence ratio $\mathcal{Z}_s/\mathcal{Z}_n$ is the false alarm probability (FAP). This is given by

$$\mathrm{FAP} = \frac{1}{1 + \mathcal{Z}_s/\mathcal{Z}_n}. \tag{11}$$

The relative log-evidence ($\log \mathcal{Z}_s - \log \mathcal{Z}_n$) is output by LALINFERENCE. The FAP can be converted into a false alarm rate (FAR) by dividing it by the length of the time window [68]. This accounts for the amount of time in which we searched for a signal in the data and assumes that all such time intervals are independent.

$$\mathrm{FAR} = \frac{1}{1 + \mathcal{Z}_s/\mathcal{Z}_n} \times \frac{1}{\Delta t}. \tag{12}$$

The time window used in our prior is $\Delta t = 0.2$ s.

We compute the Bayesian evidences of the signal plus Gaussian noise model for all simulated signals using injections at SNRs ranging from 6 to 18. Total observed masses ranged from $50 M_\odot$ to $500 M_\odot$, mass ratios were $q = \{1.25, 4\}$, and inclinations were $\theta_{JN} = \{0, \pi/3, \pi/2\}$. In Fig. 4 we show the median FAP and FAR calculated over all signals as a function of the SNR. The shaded area covers the range from minimum to maximum computed FAPs. Confident detection can be claimed for a network SNR $\gtrsim 9$,
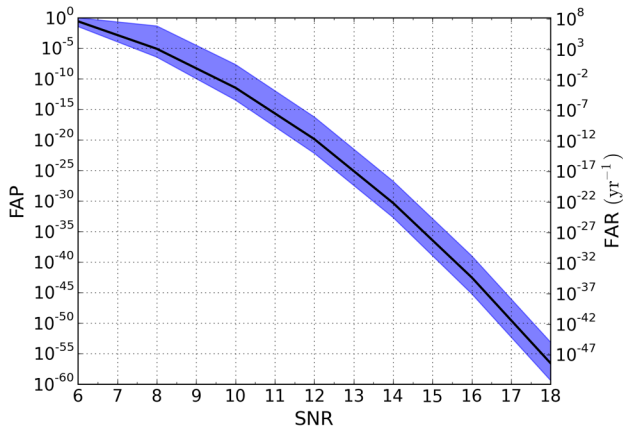
FIG. 4 (color online). False alarm probabilities and rates computed using Bayesian inference for signals buried in Gaussian noise as a function of the injected signal's SNR. The solid line is the median FAP/FAR and the shaded area covers the range from minimum to maximum values of FAP/FAR. Confident 5-σ significance detections can be claimed for SNR $\gtrsim 9$ but SNRs ~ 12 are needed in reality for the same significance in real data that is often non-Gaussian and nonstationary.

as this corresponds to a detection outside of the ± 6-σ region (FAP $< 10^{-5}$). This should be taken with a grain of salt, however, as real data will contain non-Gaussian and nonstationary noise features that will need to be addressed with noise modeling [69,70]; SNRs ~ 12 are needed in reality for the same significance in real data that is often non-Gaussian and nonstationary.

In systems where the subleading modes contribute significantly to the SNR, not including them can result in not recovering the full power of the signal. This means that using a (2,2)-only template (EOBNRv2) will yield a lower Bayesian evidence than a more complete template (EOBNRv2HM) for the same signal. This loss in evidence will lead to a greatly increased FAP and FAR. A model comparison between the two will favor the complete model when these modes are significant—inclined systems with larger mass ratios. Fig. 5 shows that in these cases the EOBNRv2HM waveform model including subleading modes will be strongly favored; when subleading modes contribute little SNR, neither waveform model is strongly favored over the other [slight preference for (2,2)-only when $\theta_{\mathrm{JN}} = 0$ and slight preference for subleading modes when $\theta_{\mathrm{JN}} > 0$ and q is close to 1].

The importance of including subleading modes in search pipelines was investigated in Ref. [47]. They found that using waveforms with subdominant modes increases the sensitive region only for high total masses ($M_{\mathrm{obs}} \gtrsim 100 M_{\odot}$) and asymmetric ($q \gtrsim 4$) IMBHBs. Furthermore, they found that the most significant gains are in regions of the parameter space with the lowest expected event rates. Although the study of Ref. [47] was limited to component masses $m_i \leq 200 M_{\odot}$ and $M_{\mathrm{obs}} < 360 M_{\odot}$, we can expect
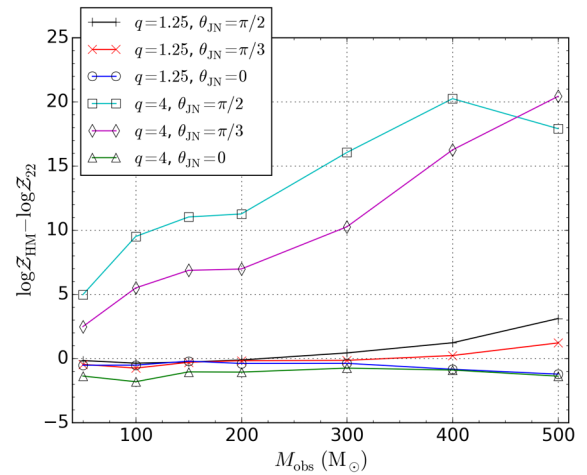

FIG. 5 (color online). We show the difference in log-evidence between using EOBNRv2HM and EOBNRv2 templates for recovering EOBNRv2HM signals. In cases with significant contribution from subleading modes the EOBNRv2HM model is strongly favored.

the trends to continue for larger masses. The result that subleading modes are significant in detection only for asymmetric and large total mass systems is consistent with our findings described in this section.

V. MEASUREMENT

After the detection of a GW signal from a binary system, we perform parameter estimation analysis, which involves producing a sufficient number of samples from the posterior distribution so that we are able to measure peaks and analyze correlations and degeneracies. Since we expect our first detections to be at just above threshold, all analyses in this section—unless otherwise stated—use injected signals with a network SNR of 12. This is achieved by adjusting the distance of the signal to obtain this exact value.

In the following sections we discuss our ability to perform parameter estimation under varying conditions. We estimate the statistical uncertainty and bias in the measurement of signal parameters; these are the width of the posterior distribution and the distance between the peak and the true values, respectively. In creating the data to be analyzed, no noise realization is added. This eliminates additional uncertainty and bias introduced by a random noise realization; zero noise is the most probable realization. This is different from averaging over many noise realizations, as the latter would result in increased uncertainty even as the biases cancel out (and would also require many more runs to be performed).

Results presented are predominantly for $q = \{1.25, 4\}$ systems. Analyses were also performed where injected waveforms had $q = \{1, 2, 3\}$; we found the results to be consistent with those discussed here. We limited $q \leq 4$ for injected signals due to the increased computational cost for higher mass-ratio waveforms.

A. Measuring variance with increasing binary's total mass

In our first set of comparisons, we study the effect of the total mass of the system on the estimation of the source's intrinsic parameters. Specifically, we investigate the statistical errors on the measurement of M_{obs}, $\mathcal{M}$, η, m_1, and m_2. Posterior distributions over $(M_{obs}, \mathcal{M}_{obs})$-space and (m_1, m_2)-space are shown for various values of M_{obs} (always using $q = 4$ and $\theta_{JN} = \pi/3$) in Fig. 6. These are summarized in the left panel of Fig. 7, which shows the
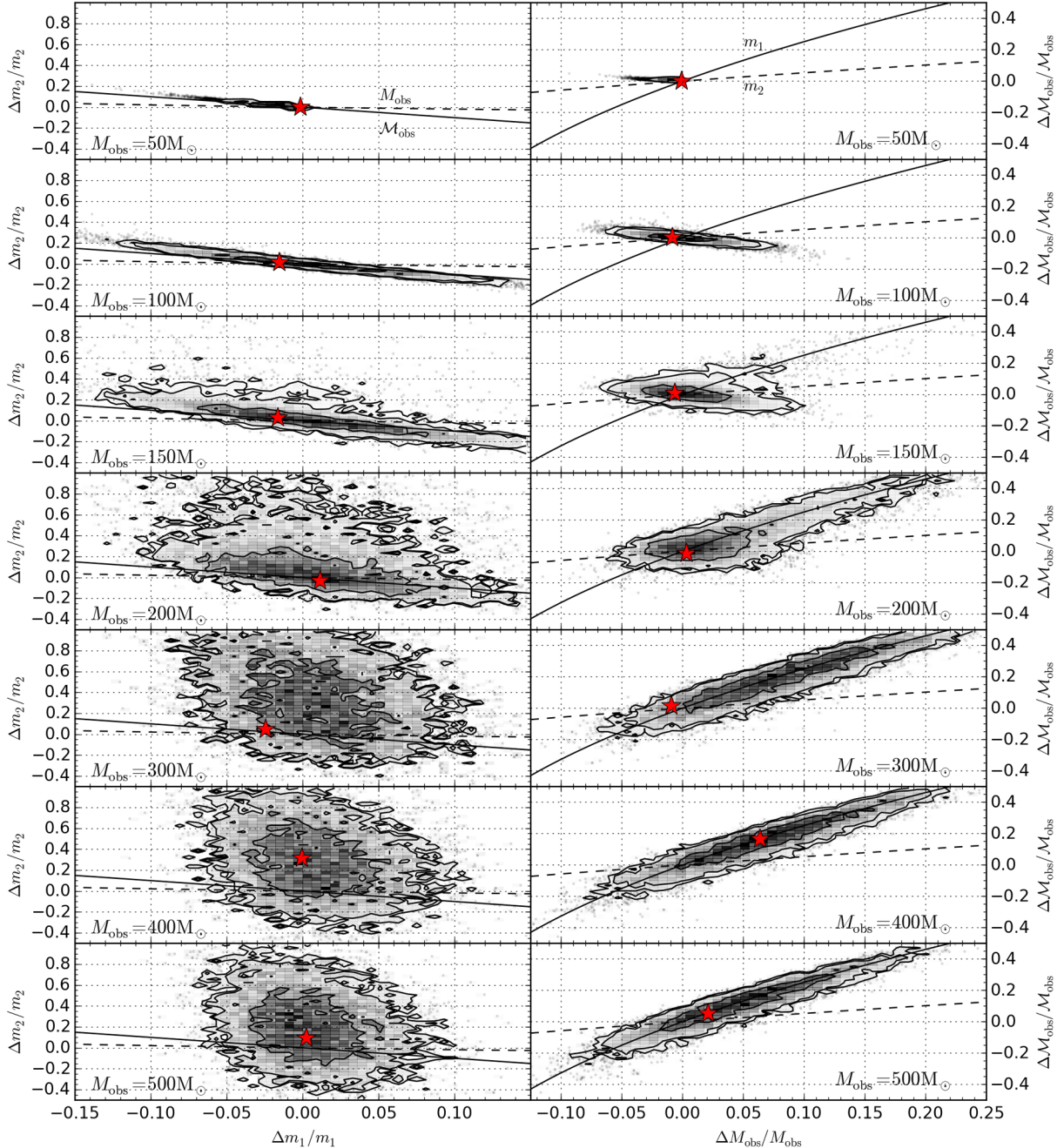

FIG. 6 (color online).   Posterior distributions of the mass estimation. All values are presented as fractional errors, i.e., $(x - x_{true})/x_{true}$. The left column displays m_2 vs. m_1 and the right column displays $\mathcal{M}_{obs}$ vs. M_{obs}. The rows are of increasing M_{obs} from $M_{obs} = 50 M_\odot$ at the top to $M_{obs} = 500 M_\odot$ at the bottom. For all systems, $q = 4$ ($\eta = 0.16$) and $\theta_{JN} = \pi/3$. The star indicates the point with highest $\log \mathcal{L}$ and the contours are at 50%, 90%, and 95% credible levels (inside to outside). In the left column, the solid lines are of constant M_{obs} and the dashed lines are constant $\mathcal{M}_{obs}$; in the right column, solid is constant m_1 and dashed is constant m_2. In all cases the lines intersect the true values at $(x, y) = (0, 0)$.
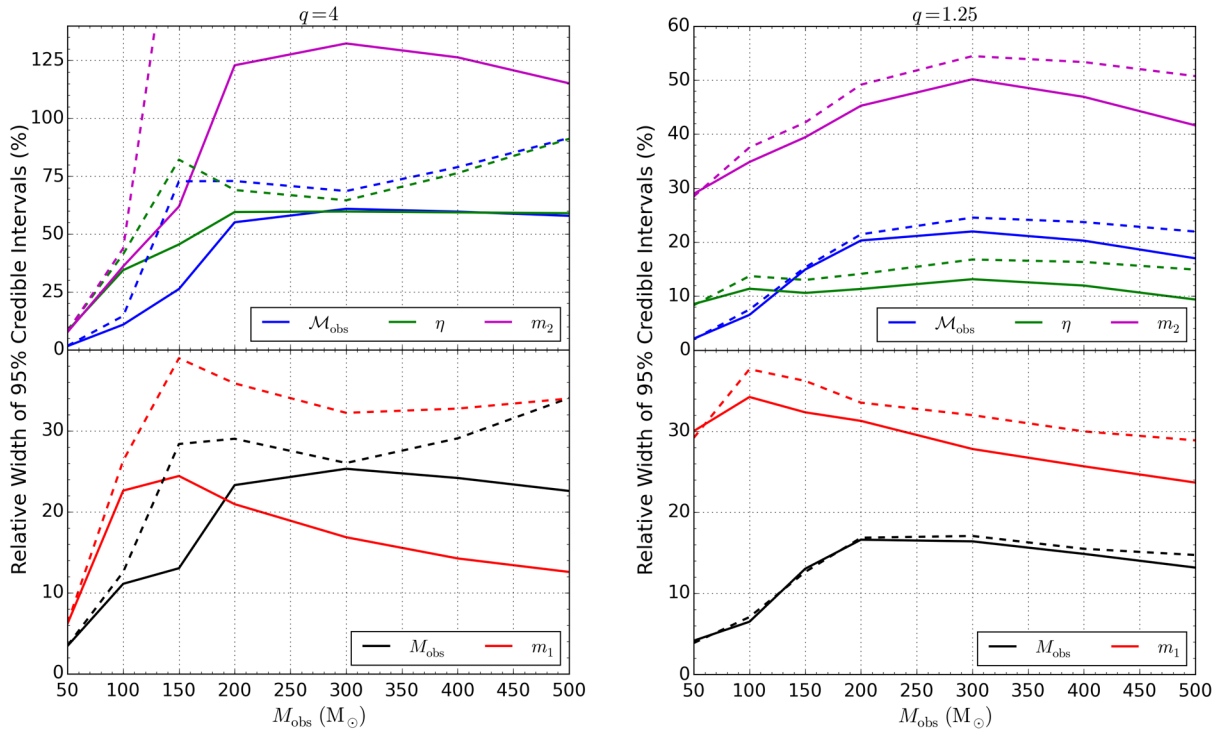
FIG. 7 (color online).   Uncertainty in the measurement of different mass parameters: $M_{\rm obs}$, $\mathcal{M}$, and η. Results here are for a system with (left panel) $q = 4$ ($\eta = 0.16$) and (right panel) $q = 1.25$ ($\eta = 0.247$). In both cases, $\theta_{\rm JN} = \pi/3$ and SNR $= 12$. The solid lines are for templates with subleading modes and the dashed lines are for templates with the (2,2) mode only. The relative width is given by $\left(x_{97.5\%} - x_{2.5\%}\right)/x_{\rm true}$.

relative widths of the 95% (± 2-σ) credible intervals (i.e., $(x_{97.5\%} - x_{2.5\%})/x_{\rm true}$) for the various mass parameters. At the lower mass end ($M_{\rm obs} = 50{\rm M}_\odot$), uncertainty is low due to how well the chirp mass $\mathcal{M}_{\rm obs}$ is measured from the inspiral phase of a waveform. As the total mass increases, the uncertainty increases and for $M_{\rm obs} \geq 150{\rm M}_\odot$ the uncertainty in $\mathcal{M}_{\rm obs}$ is similar to or greater than that in $M_{\rm obs}$. This change is due to less inspiral signal being present in the most sensitive band of the detector; the ringdown is predominantly dependent on $M_{\rm obs}$ and therefore this parameter is measured more accurately. However, the inspiral measures $\mathcal{M}_{\rm obs}$ better than the ringdown measures $M_{\rm obs}$, so the resulting uncertainty is larger. Above $M_{\rm obs} = 300{\rm M}_\odot$, the uncertainty decreases slightly; this is due to the ringdown matching up better with the minimum of the advanced LIGO/Virgo PSD and the subleading modes moving into more sensitive regions of the PSD.

When these same systems are face-on ($\theta_{\rm JN} = 0$) or have lower q (more equal component masses), the uncertainties for the (2,2)-only waveform closely resemble those for the waveform with all modes, just a little larger. This can be seen in the right panel of Fig. 7 and it is what would be expected for systems with little contribution from the subleading modes. In all cases, the templates that include subleading modes of radiation have lower uncertainty than those using only the (2,2)

mode. Additionally, for inclined and asymmetric systems, as $M_{\rm obs}$ increases from $300{\rm M}_\odot$ to $500{\rm M}_\odot$, the uncertainty when using (2,2)-only templates grows significantly while that from using templates with subleading modes slightly decreases. This is due to the fact that the subleading modes provide information about the mass ratio of the system in their relative amplitudes and phases. This information contained in the subdominant modes breaks the model degeneracies and allows us to better infer the component masses as the ringdown phase of the waveform enters the most sensitive region of the PSD. These results can also be seen in Fig. 6. Being able to accurately measure the component masses is important in allowing us to make inferences on the source population of these massive BHs [10].

Thus, we observe that at a SNR of 12 uncertainties for $M_{\rm obs}$ can reach $\sim$20–25% in asymmetric binaries while uncertainty in $\mathcal{M}_{\rm obs}$ reaches up to $\sim$50–60% (these numbers are $\sim$17% vs. $\sim$22% in more symmetric mass ratio binaries).

In the Appendix, we provide summary tables of relative 95% credible intervals for measurements of the masses, luminosity distance, and coalescence time. These are given over a range of SNRs for two mass ratios ($q = \{1.25, 4\}$) and several observed total masses at the inclinations of $\theta_{\rm JN} = \{\pi/3, 0\}$.

B. Measuring degeneracies with increasing binary's total mass

As the IMBHB systems increase in total mass, there are distinct changes in the two-dimensional posterior probability distributions. As the inspiral phase evolution strongly constrains $\mathcal{M}_{obs}$ and η, in that order, lower mass systems will have degeneracies that follow contours in these parameters. With increasing total mass, however, the inspiral becomes less important and the merger-ringdown part of the signal contributes significantly or dominantly to the SNR. This is most well described by M_{obs} with much weaker dependence on η. Thus, we expect there to be a change in the degeneracies present in the mass estimation. The inspiral dependency on $\mathcal{M}_{obs}$ can be seen in the PN inspiral waveforms (see Ref. [71]); PN approximants are accurate for early inspiral when the BHs are sufficiently far from merger. The dependency on M_{obs} of the ringdown is similarly given by the quasinormal mode decomposition derived in Ref. [72] and implemented in the EOB waveform models used in our study [5].

This change in the optimally measured parameters as M_{obs} increases can be observed in Fig. 6. In the right column, we show the posterior distribution of the masses, parametrized as M_{obs} and $\mathcal{M}_{obs}$, over a range of total masses for an asymmetric system ($q = 4$,

$\eta = 0.16$) viewed at an angle ($\theta_{JN} = \pi/3$). In the top row, $M_{obs} = 50M_{\odot}$ and we can see that the principal measurement is of the chirp mass $\mathcal{M}_{obs}$—posterior samples and contours lie along a line of near-constant $\mathcal{M}_{obs}$. As M_{obs} increases, at $M_{obs} = 150M_{\odot}$ a second principal direction of degeneracy becomes evident. This is due to a different combination of the mass parameters becoming increasingly constrained relative to the others and realizing a new degeneracy in the measurement.

These observations confirm what we see in the one-dimensional posteriors in Fig. 7. The chirp mass $\mathcal{M}_{obs}$ is initially measured to lower fractional error than the total mass M_{obs}; as M_{obs} increases the uncertainty grows much faster in $\mathcal{M}_{obs}$ than it does in M_{obs}. The small decrease in uncertainty at the higher masses is also visible as the contours shrink slightly. We are now able to see in Fig. 6 that this increase in uncertainty is accompanied by a changing of the dominant degeneracy in the parameters of the waveform model.

C. Importance of including subleading modes

As discussed previously, in addition to the leading (2,2) mode, the EOBNRv2HM waveform model also includes subleading modes (2,1), (3,3), (4,4), and (5,5), which introduce additional structure to the waveform and
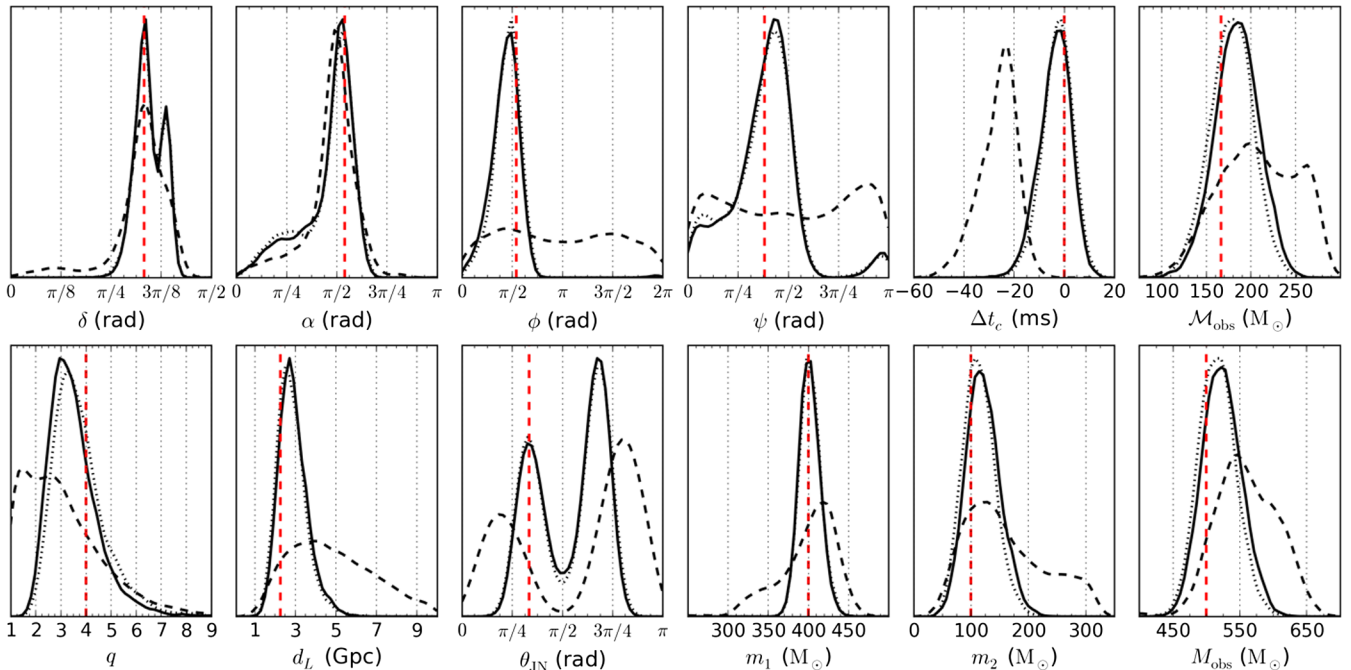

FIG. 8 (color online).   One-dimensional posterior distributions for all parameters for an injected signal with $M_{obs} = 500M_{\odot}$, $q = 4$, $\theta_{JN} = \pi/3$, and SNR = 12. Posteriors are compared for (solid) the EOBNRv2HM waveform model which includes subleading modes of radiation, (dashed) the EOBNRv2 waveform model which includes only the (2,2) mode, and (dotted) the EOBNRv2HM waveform model along with a different prior distribution that is flat in $(\log(\mathcal{M}_{obs}), \eta)$ instead of flat in (m_1, m_2). The vertical dashed red lines indicate the true (injected) value of each parameter.
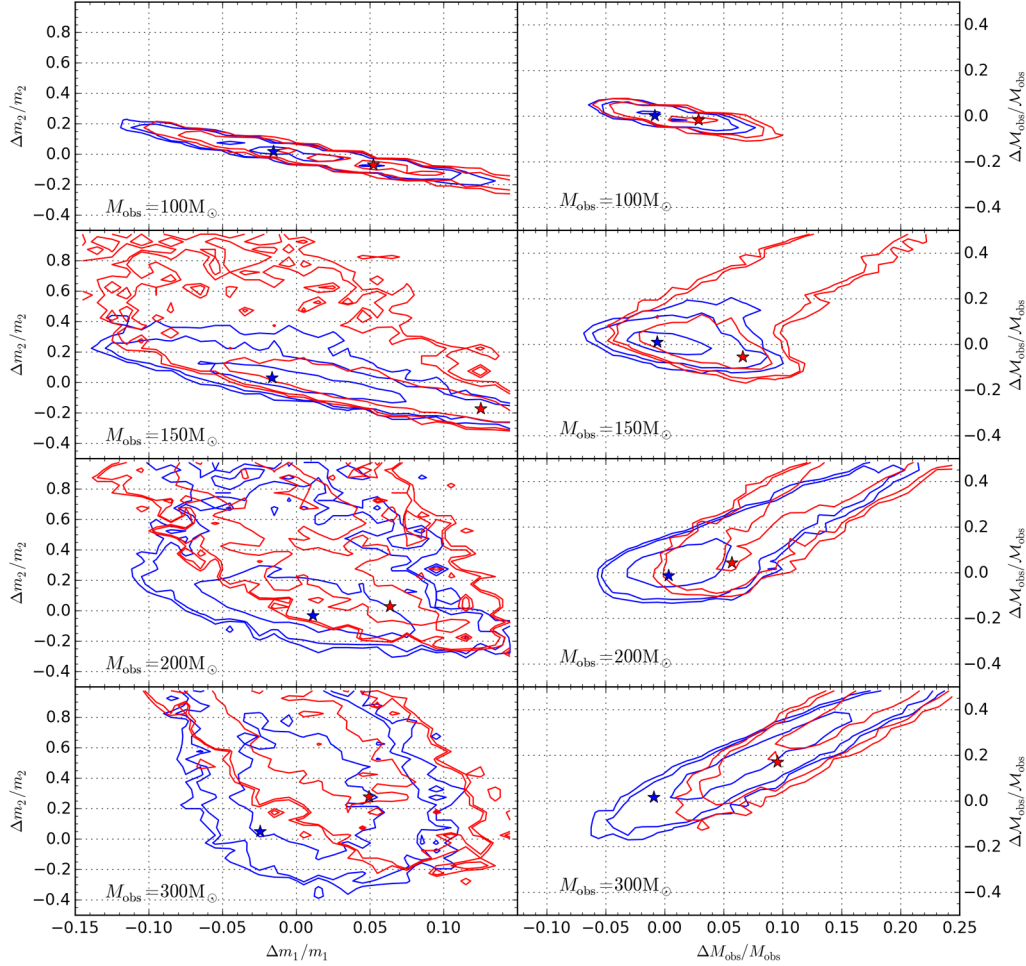
FIG. 9 (color online).   Posterior distributions of the mass estimation. All values are presented as fractional errors, i.e., $(x - x_{\text{true}})/x_{\text{true}}$. The left column displays m_2 vs. m_1 and the right column displays $\mathcal{M}_{\text{obs}}$ vs. M_{obs}. The rows are of increasing M_{obs} from $M_{\text{obs}} = 100 \text{M}_\odot$ at the top to $M_{\text{obs}} = 300 \text{M}_\odot$ at the bottom. For all systems, $q = 4$ ($\eta = 0.16$) and $\theta_{\text{JN}} = \pi/3$. The asterisks indicate the point with highest $\log \mathcal{L}$ and the contours are at 50%, 90%, and 95% credible levels (inside to outside). Blue contours use EOBNRv2HM as a waveform template while red contours use EOBNRv2, which only includes the leading (2,2) mode.

improve faithfulness to NR waveforms. This increased structure is important as the relative amplitudes and phasing of the additional modes introduce information about the source masses. In the ringdown phase, the additional modes further constrain the mass and spin of the final BH. This structure creates variation in waveforms as initial component masses are varied, thereby allowing Bayesian inference to measure the masses more accurately and precisely as seen in Figs. 7, 8, and 9.

The modes' structure also contains angular dependence on the inclination of the system to the detector, θ_{JN}, the orientation of the orbit in the plane of the sky (polarization), ψ, and the orbital phase of the binary, ϕ. This structure is present for the primary (2,2) mode, but the introduction of additional modes breaks degeneracies in the observed waveform as these angles vary.

Improvements in measurement of the masses and orientation angles can all be observed in the example presented in Fig. 8. This figure compares one-dimensional posterior distributions for the case of an injected signal with $M_{\text{obs}} = 500 \text{M}_\odot$, $q = 4$, and $\theta_{\text{JN}} = \pi/3$. The solid black line shows the posterior distribution for the waveform template model including subleading modes (EOBNRv2HM) and the dashed line is for the waveform template model including only the leading (2,2) mode (EOBNRv2). In both cases, the signal injected into the data contained the subleading modes—in nature, all modes of radiation are present.

For parameter estimation, the presence of subleading modes means that as the angles θ_{JN}, ψ, and ϕ vary, there is increased variation of the waveform. This variation is more prominent for unequal mass binaries and binaries not observed face-on or face-off ($\theta_{\text{JN}} = \{0, \pi\}$), as the subleading modes will have more significant

contributions to the SNR. The increased variation allows for more accurate measurement of θ_{JN} and breaks degeneracies in ψ and ϕ to allow these two angles to be measured. As M_{obs} and θ_{JN} are strongly correlated with the luminosity distance d_L via the amplitude of the waveform, measuring the former two more accurately means that the latter will be measured more accurately as well.

The measurement of the coalescence time t_c is offset when using only the leading mode; this is likely due to slight errors in measuring the sky position of the source and adjustments in order to align the peak amplitude of the waveform at merger.

With the additional information provided by the subleading modes in the EOBNRv2HM model, posterior distributions for all mass parameters are narrower and better centered on the true values. Most notably, the subleading modes and their relative amplitudes differentiate better between waveforms with the same total mass, but different mass ratios. The system injected in the analysis shown in Fig. 8 has very high M_{obs} so the merger and ringdown provide the majority of the SNR. The observed improvement is thus due to a waveform degeneracy in the mass of the final BH that can be broken when we are able to measure the final mass and spin of the BH more precisely. These depend strongly on the mass ratio of the initial components and are further realized in the relative amplitudes of the subleading modes. The improved measurement of initial mass values from using subleading modes can also be seen in Fig. 9, where we compare two-dimensional posteriors in the masses between EOBNRv2HM and EOBNRv2 waveform models over a range of M_{obs} ($q = 4$ and $\theta_{JN} = \pi/3$). Note that when $M_{obs} = 100M_{\odot}$, the posteriors are nearly identical. However, with increasing M_{obs}, the late inspiral, merger, and ringdown become increasingly important. The parameter estimation bias and loss of SNR is evident when using only the leading mode as the posteriors do not necessarily peak at or strongly support the true values and the confidence intervals are considerably larger.

As the observed total mass increases, it is very difficult to measure the mass ratio q (or η) if the source is face-on. Indeed, in this case the subdominant modes are not significant; we find that the posteriors are identical and do not change much with respect to the true q. However, when $\theta_{JN} = \pi/3$ or $\pi/2$, because of the presence of the subleading modes, it is possible to measure q, although the influence of the prior is still evident in tending toward smaller values. In Ref. [10], the authors determine that IMBHBs formed from stellar-origin massive BHs will likely have mass ratios $q \lesssim 1.25$. We find that for values of $q \geq 2$, in more massive ($M_{obs} \geq 300M_{\odot}$) and inclined systems, we will be able to say that $q > 1.25$ with certainty $> 90\%$.

In summary, we find that the inclusion of subleading modes of gravitational radiation improves the accuracy and precision of the estimation of the source mass parameters as well as some extrinsic parameters, such as distance and orientation angles. They are significant for asymmetric and inclined binaries where they contribute more to the signal's SNR.

D. Effect of priors

So far, in all of the analysis runs, we have used a very large prior on the component masses, which was flat in (m_1, m_2) space. However, one could argue for other reasonable prior distributions on the masses. One such alternative is to use a prior that is flat in $\log(\mathcal{M}_{obs})$. The quantity $\log(\mathcal{M}_{obs})$ is used because $\mathcal{M}_{obs}$ is a scaling factor for the waveform amplitude and $\log(\mathcal{M}_{obs})$ is the so-called Jeffreys prior. Additionally, we employ a prior that is flat in η for the second mass parameter.

We ran multiple analyses with this second prior option, which is flat in $(\log(\mathcal{M}_{obs}), \eta)$ and find that even at a SNR of 12 the strength of the signal is sufficient to render the different prior distribution a minimal factor. This can be seen in Fig. 8, where we show the one-dimensional posteriors from a single analysis. More specifically, we display in dotted lines the 1D posteriors of a run with EOBNRv2HM waveform model that uses the alternative prior, to be compared with the solid lines from the run with the original prior. The lines are nearly identical, with differences much smaller than those from using the EOBNRv2 waveform; these differences from the alternative prior will continue to decrease as the SNR is increased.

E. Comparison to previous parameter-estimation work with inspiral-merger-ringdown waveforms

In an earlier work, Ajith and Bose [30] used inspiral-merger-ringdown phenomenological waveform models (IMRPhenomA) to perform a study similar to ours, but mainly focusing on understanding how uncertainties are reduced when merger and ringdown phases are included. Their study did not include subleading modes. They examined the statistical error in parameter estimation as given by the Fisher information matrix[4] and MCMC analyses. Our uncertainties calculated using EOBNRv2 templates [(2,2) mode only] are a factor of a few larger than those given in Table 1 of Ref. [30] for SNR = 10, $M_{obs} = \{100, 200\}M_{\odot}$, and $\eta = \{0.25, 0.16\}$ (e.g., Ref. [30] quotes relative uncertainties of 2.39% and 3.57% for M_{obs}

---

[4]The Fisher information matrix measures covariances analytically. The square root of the diagonal elements of the inverse of the Fisher matrix gives a lower bound on the standard deviation of the posterior for the parameters. In the limit of large SNR, this estimate becomes exact.

in cases with $q = 1$ and $M_{obs} = 100 M_\odot$ or $M_{obs} = 200 M_\odot$; we measure uncertainties of 4.01% and 9.66% in these same cases). The discrepancy in uncertainties is partly a result of the fact that in Ref. [30], the authors maximize their likelihood function over t_c and ϕ and only perform a single-detector search using an "effective" distance that folds in sky position and binary inclination effects; both of these choices have the effect of fixing values for parameters that we allow to vary in our more general analysis, thus introducing additional uncertainty. Furthermore, we use EOBNRv2HM waveforms as injections, as these most closely model NR waveforms, and our EOBNRv2 templates differ from IMRPhenomA ones, the former being more faithful to NR waveforms [54]. Despite those differences, the quantitative measurements are in general agreement and we also find agreement in the qualitative aspects of increasing uncertainty in mass parameters with increasing M_{obs}. We report our own estimations of the uncertainty in the Appendix, using the full EOBNRv2HM waveform model.

In Ref. [32], Littenberg et al. examined systematic and statistical errors of EOBNR waveforms to assess whether those waveforms are indistinguishable from the NR waveforms used to calibrate them. The authors employed both EOBNRv2 and EOBNRv2HM templates to recover waveforms generated by NR simulations and, when using subleading modes, find systematic errors to be comparable to or less than statistical errors for mass ratios up to $q = 6$ and SNRs up to 50. We find statistical errors comparable to the ones of Ref. [32] for analyses run in common. Our results on the importance of subleading modes for unequal-mass and inclined $(\theta_{JN} > 0)$ systems reaffirm their findings.

Varma et al. [37] built on Refs. [32,47]. They used as targets "hybrid" waveforms constructed by attaching PN inspiral/EOB waveforms to NR merger-ringdown waveforms, and as templates EOBNRv2 waveforms. Instead of examining only a few points in parameter space, they ran many simulations in order to average over relative orientation angles. Statistical errors were computed with the Fisher information matrix. Confirming previous work, they found that subleading modes are more important for parameter estimation when $M_{obs} \geq 150 M_\odot$ and $q \geq 4$ and important for detection when $M_{obs} \geq 100 M_\odot$ and $q \geq 6$ (see Fig. 1 of Ref. [37]). In contrast, our paper employs the full EOBNRv2HM waveforms and uses Bayesian analysis, and it extends the study to higher M_{obs}.

Bose et al. [31] focused on the importance of including merger and ringdown phases of the waveform. They analyzed the recovery of inspiral-merger-ringdown waveforms with PN inspiral waveforms and found that at masses as low as $M_{obs} = 50 M_\odot$ there are serious systematic errors and an increase in statistical errors due to the loss in SNR. This result is consistent with our analysis showing the significant amount of signal power present in the merger and ringdown phases of the waveform at $M_{obs} = 50 M_\odot$ and above.

F. Astrophysical implications

As mentioned in Sec. I, the merger rate of IMBHBs is currently highly uncertain. Consequently, detection of a single event will immediately confirm the existence of these systems and constrain their rate. In the absence of detection the upper limits reached could be used to rule out some of the models.

As shown in Fig. 1, ground-based detectors will have the greatest distance reach for equal-mass IMBHBs of observed total mass of $\sim 400 M_\odot$. The distance reach for such systems will be ~ 6.5 Gpc or $z \simeq 1$. We find that the comoving volume averaged over all source orientations and weighted by the antenna pattern functions of the advanced LIGO-Virgo network is ~ 150 Gpc^3, larger by a factor ~ 1.8 than that in Ref. [10]. This difference can be explained because, as opposed to Ref. [10], we consider a detector network (which increases the reach) and use a different SNR (which decreases the reach). After five years of nonobservation of IMBHBs a rate upper limit of 4×10^{-11} Gpc^{-3} yr^1 can be achieved, which is smaller than the rates for most formation models discussed in Ref. [10–12]. For a binary of same total mass, $\sim 400 M_\odot$, but mass ratio $q = 4$, the reach when including subleading modes is smaller by a factor of 1.5 (see Fig. 1) and the upper limit will be larger by a factor 3.375, i.e., 1.35×10^{-1} Gpc^{-3} yr^1. Neglecting the subleading modes worsens the upper limit by a factor 2.4. However, Ref. [47] showed that in a realistic search the improvement when including subleading modes is significant only for mass ratios larger than ~ 4.

An important question in cosmology is the mass function of IMBHs. Routine detection of IMBHs will help us measure the mass function of component BHs that form merging binaries and this should be a proxy for the mass function of IMBHs in the Universe, unless IMBHBs are formed selectively from a subpopulation of IMBHs. The component masses of a binary system are strongly correlated and it is not possible to measure them accurately while using only the dominant mode; subleading modes break this degeneracy, especially in the case of asymmetric binaries for which the mass ratio q is large, helping us measure the component masses more accurately. In particular (see Fig. 7), the 95% credible interval in the measurement of the heavier companion can be 10% to 25%, while the lighter component is measured within 10% to 125%, depending on the total mass of the binary. These results are far better than what might be possible by electromagnetic observations of such binary systems. Therefore, advanced detectors provide the most robust way of determining the mass function across the range of masses from $50 M_\odot$ to $500 M_\odot$. A related question is the

mass function of IMBHBs. Referring to Fig. 7, the total mass is determined to within a few percent in the case of lighter binaries of $50M_\odot$ to within 15–25% for the heaviest systems of $500M_\odot$ that we consider. Thus, advanced detectors should help determine the mass function of IMBHBs.

VI. CONCLUSIONS

In this paper we used state-of-the-art waveform models for inspiral-merger-ringdown phases of evolution to estimate uncertainties in parameters of IMBHBs with total mass $M_{\mathrm{obs}} = 50M_\odot$–$500M_\odot$ and mass ratio $q = 1$–4. Because for these systems the majority of the SNR is accumulated during the last stages of inspiral, merger and ringdown phases, where subleading modes can become comparable to the leading (2,2) mode, we also included in the analysis four subleading modes, i.e., (2,1), (3,3), (4,4) and (5,5). In particular, we employed the EOBNRv2 and EOBNRv2HM waveform models in LAL.

Using a Bayesian analysis, we found that for unequal-mass systems and inclined binaries subleading modes improve the measurement of the mass parameters and break degeneracies in distance and orientation angles (see Sec. V C). As the binary's total mass increases, the merger and ringdown phases dominate the SNR. Since for such high-mass binaries the signal resembles a burst, the measurement will extract the dominant frequency of oscillation of the signal, which depends primarily on the total mass, thus the uncertainty in total mass becomes smaller than the uncertainty in the chirp mass (see Sec. V A, Fig. 7 and Tables I and II). In contrast, for lower total masses, the SNR accumulates over many cycles of inspiral and the chirp mass is better measured. The presence of subleading modes is less crucial for comparable-mass systems and face-on binaries (see Sec. V A, Fig. 7 and Table I). Inclusion of subleading modes allows for improved measurement of the mass ratio for asymmetric and inclined systems (see Table II). Finally, as discussed in Sec. V F, GW observations of IMBHBs will demonstrate the existence and shed light on the demographics of IMBHs, even if component masses will be measured only with a fractional error of (several) tens of percent.

Our analysis was restricted to nonspinning IMBHs and explored only part of the parameter space. These limitations were a consequence of the fact that EOBNR waveform models are expensive to generate for Bayesian analyses. Higher-mass binaries ($M_{\mathrm{obs}} \sim 400M_\odot$) take tens to hundreds of milliseconds to generate, while lower-mass binaries ($M_{\mathrm{obs}} \sim 50M_\odot$) will require up to tens of seconds;

computational time will quickly add up as 10^6–10^7 waveform computations are required for a complete analysis. This cost is compounded by the requirements both for long segments to enclose the entire waveform while in-band (long due to the low minimum frequency) and a high sampling rate in order to include the subleading modes in the ringdown signal. Recently, reduced-order models (ROM) have been developed for EOBNR waveforms, either for spinning, nonprecessing systems [73] or nonspinning, but with subleading-mode waveforms [74]. Future investigations could employ these faster template families.

While completing this work, we became aware of the study of Ref. [75], which includes the effect of nonprecessing spins using a ROM built on the SEOBNRv2 template family [73,76], while discarding the subdominant modes.

APPENDIX: SUMMARY OF MEASUREMENTS

In this section we present tables of the 95% credible intervals for five of the measured parameters: M_{obs}, η, $\mathcal{M}_{\mathrm{obs}}$, d_L, and t_c. Results are presented for two mass ratios ($q = 1.25$ and $q = 4$) and for two inclinations ($\theta_{\mathrm{JN}} = \pi/3$ and $\theta_{\mathrm{JN}} = 0$). For all parameters except t_c, these values are scaled by their true values and converted into percentages. Uncertainty in t_c is presented in ms. Table I presents values for $q = 1.25$ and Table II presents results for $q = 4$. For the two inclinations, results are side-by-side, with $\theta_{\mathrm{JN}} = 0$ in parentheses.

TABLE I.   Measurement uncertainties for `EOBNRv2HM` signals with `EOBNRv2HM` templates. The values are the (relative) widths of the 95% credible intervals from the one-dimensional marginalized posterior distributions, scaled by the true value when indicated. For all runs, $q = 1.25$ ($\eta = 0.247$). $\theta_{JN} = \pi/3$ and $\theta_{JN} = 0$ results are shown side-by-side, with the latter in parentheses.

SNR	$M_{obs} = 50M_\odot$	$100M_\odot$	$150M_\odot$	$200M_\odot$	$300M_\odot$	$400M_\odot$	$500M_\odot$
				$\Delta M_{obs}/M_{obs}$			
6	16.810 (16.658)	6.895 (6.655)	2.607 (2.815)	0.612 (0.610)	0.479 (0.515)	0.472 (0.497)	0.400 (0.410)
8	16.756 (16.464)	0.159 (0.158)	0.280 (0.285)	0.288 (0.287)	0.262 (0.251)	0.239 (0.255)	0.213 (0.214)
10	0.052 (0.049)	0.086 (0.090)	0.180 (0.178)	0.202 (0.201)	0.201 (0.200)	0.180 (0.181)	0.155 (0.159)
12	0.041 (0.040)	0.065 (0.064)	0.130 (0.130)	0.166 (0.161)	0.164 (0.169)	0.149 (0.150)	0.132 (0.125)
14	0.031 (0.033)	0.050 (0.050)	0.100 (0.102)	0.137 (0.135)	0.143 (0.139)	0.128 (0.124)	0.113 (0.105)
16	0.027 (0.028)	0.042 (0.045)	0.080 (0.082)	0.116 (0.118)	0.132 (0.129)	0.109 (0.105)	0.090 (0.088)
18	0.025 (0.025)	0.038 (0.038)	0.070 (0.074)	0.100 (0.104)	0.113 (0.107)	0.097 (0.087)	0.083 (0.075)
				$\Delta\eta/\eta$			
6	0.874 (0.872)	0.866 (0.863)	0.709 (0.725)	0.488 (0.427)	0.475 (0.484)	0.512 (0.510)	0.520 (0.524)
8	0.870 (0.871)	0.201 (0.191)	0.177 (0.181)	0.182 (0.198)	0.218 (0.227)	0.221 (0.218)	0.203 (0.186)
10	0.109 (0.104)	0.135 (0.144)	0.126 (0.130)	0.132 (0.131)	0.158 (0.146)	0.136 (0.153)	0.131 (0.097)
12	0.085 (0.082)	0.114 (0.112)	0.106 (0.099)	0.113 (0.107)	0.131 (0.129)	0.120 (0.111)	0.094 (0.075)
14	0.063 (0.067)	0.086 (0.093)	0.090 (0.086)	0.089 (0.092)	0.108 (0.100)	0.100 (0.082)	0.065 (0.053)
16	0.055 (0.057)	0.077 (0.086)	0.077 (0.073)	0.080 (0.078)	0.107 (0.096)	0.082 (0.061)	0.054 (0.038)
18	0.049 (0.050)	0.071 (0.072)	0.070 (0.069)	0.072 (0.073)	0.085 (0.074)	0.069 (0.049)	0.045 (0.034)
				$\Delta\mathcal{M}_{obs}/\mathcal{M}_{obs}$			
6	16.913 (16.613)	6.594 (6.315)	0.995 (1.293)	0.605 (0.620)	0.603 (0.602)	0.626 (0.634)	0.627 (0.614)
8	16.662 (16.350)	0.169 (0.182)	0.312 (0.324)	0.333 (0.338)	0.344 (0.344)	0.347 (0.357)	0.304 (0.292)
10	0.029 (0.027)	0.091 (0.099)	0.199 (0.200)	0.237 (0.239)	0.269 (0.263)	0.240 (0.250)	0.213 (0.197)
12	0.021 (0.021)	0.065 (0.068)	0.149 (0.146)	0.203 (0.195)	0.220 (0.223)	0.203 (0.199)	0.170 (0.150)
14	0.015 (0.016)	0.049 (0.052)	0.116 (0.118)	0.163 (0.166)	0.192 (0.190)	0.178 (0.157)	0.138 (0.123)
16	0.013 (0.013)	0.043 (0.043)	0.091 (0.095)	0.140 (0.142)	0.180 (0.173)	0.146 (0.128)	0.110 (0.098)
18	0.011 (0.012)	0.037 (0.036)	0.081 (0.084)	0.125 (0.130)	0.149 (0.137)	0.127 (0.105)	0.096 (0.086)
				$\Delta d_L/d_L$			
6	1.819 (2.438)	1.252 (1.649)	0.843 (1.078)	0.629 (0.835)	0.469 (0.655)	0.449 (0.615)	0.510 (0.658)
8	2.423 (3.066)	1.470 (1.982)	1.229 (1.569)	0.873 (1.252)	0.673 (0.932)	0.687 (0.911)	0.803 (1.090)
10	1.215 (1.616)	1.211 (1.559)	1.213 (1.628)	1.179 (1.578)	0.973 (1.319)	0.973 (1.375)	1.183 (1.560)
12	1.140 (1.513)	1.084 (1.463)	1.104 (1.526)	1.133 (1.559)	1.164 (1.576)	1.270 (1.561)	1.390 (1.461)
14	1.045 (1.333)	0.980 (1.399)	1.002 (1.417)	1.030 (1.467)	1.106 (1.404)	1.234 (1.245)	1.235 (1.009)
16	0.970 (1.418)	0.896 (1.365)	0.959 (1.430)	1.004 (1.423)	1.036 (1.307)	1.035 (1.010)	0.979 (0.821)
18	0.978 (1.386)	0.895 (1.373)	0.982 (1.378)	0.991 (1.337)	0.976 (1.118)	0.923 (0.846)	0.808 (0.688)
				Δt_c (ms)			
6	187.8 (188.9)	174.7 (173.3)	48.3 (56.5)	28.0 (26.2)	34.8 (34.4)	44.1 (44.4)	46.1 (48.8)
8	191.3 (190.7)	6.9 (6.8)	11.3 (11.6)	14.4 (14.8)	20.9 (19.9)	26.0 (26.2)	30.6 (29.5)
10	3.5 (3.2)	4.8 (4.8)	8.1 (7.6)	10.9 (10.5)	16.3 (15.8)	21.5 (20.2)	24.0 (22.8)
12	3.0 (2.7)	4.0 (3.9)	6.3 (6.2)	9.1 (8.9)	13.8 (13.1)	17.7 (16.3)	19.7 (18.1)
14	2.5 (2.2)	3.4 (3.1)	5.1 (5.0)	7.5 (7.3)	11.5 (11.3)	15.2 (13.6)	16.4 (14.3)
16	2.2 (1.9)	2.9 (2.6)	4.3 (4.3)	6.6 (6.6)	10.8 (9.8)	12.6 (11.1)	14.1 (12.3)
18	2.0 (1.7)	2.6 (2.5)	3.8 (3.8)	5.6 (5.8)	9.1 (8.3)	11.3 (9.6)	12.2 (10.5)

TABLE II. Measurement uncertainties for `EOBNRv2HM` signals with `EOBNRv2HM` templates. The values are the (relative) widths of the 95% credible intervals from the one-dimensional marginalized posterior distributions, scaled by the true value when indicated. For all runs, $q = 4$ ($\eta = 0.16$). $\theta_{JN} = \pi/3$ and $\theta_{JN} = 0$ results are shown side-by-side, with the latter in parentheses.

SNR	$M_{obs} = 50M_\odot$	$100M_\odot$	$150M_\odot$	$200M_\odot$	$300M_\odot$	$400M_\odot$	$500M_\odot$
				$\Delta M_{obs}/M_{obs}$			
6	16.206 (17.067)	7.659 (7.722)	3.378 (3.896)	1.821 (2.195)	0.966 (1.091)	0.822 (0.930)	0.586 (0.690)
8	16.749 (16.519)	0.336 (0.452)	0.523 (0.626)	0.417 (0.419)	0.362 (0.354)	0.334 (0.320)	0.324 (0.314)
10	15.992 (0.047)	0.138 (0.136)	0.298 (0.229)	0.310 (0.260)	0.292 (0.258)	0.269 (0.262)	0.263 (0.244)
12	0.034 (0.033)	0.111 (0.102)	0.130 (0.110)	0.233 (0.175)	0.253 (0.212)	0.242 (0.214)	0.226 (0.203)
14	0.028 (0.025)	0.091 (0.082)	0.098 (0.084)	0.176 (0.115)	0.220 (0.170)	0.212 (0.174)	0.182 (0.167)
16	0.021 (0.021)	0.078 (0.068)	0.084 (0.068)	0.111 (0.081)	0.196 (0.147)	0.185 (0.153)	0.172 (0.144)
18	0.218 (0.044)	0.072 (0.061)	0.075 (0.058)	0.085 (0.065)	0.173 (0.124)	0.163 (0.128)	0.142 (0.122)
				$\Delta\eta/\eta$			
6	1.347 (1.348)	1.343 (1.342)	1.290 (1.314)	1.140 (1.233)	1.035 (1.066)	1.063 (1.043)	1.021 (1.021)
8	1.345 (1.349)	0.817 (0.824)	0.785 (0.826)	0.753 (0.771)	0.717 (0.776)	0.693 (0.744)	0.720 (0.775)
10	1.346 (0.126)	0.478 (0.443)	0.714 (0.623)	0.705 (0.650)	0.648 (0.627)	0.666 (0.645)	0.641 (0.645)
12	0.082 (0.079)	0.344 (0.308)	0.455 (0.389)	0.595 (0.490)	0.597 (0.539)	0.594 (0.551)	0.590 (0.553)
14	0.062 (0.057)	0.272 (0.245)	0.348 (0.295)	0.492 (0.354)	0.547 (0.455)	0.541 (0.459)	0.497 (0.473)
16	0.047 (0.047)	0.227 (0.196)	0.288 (0.237)	0.369 (0.279)	0.503 (0.384)	0.502 (0.412)	0.468 (0.408)
18	0.223 (0.123)	0.203 (0.170)	0.255 (0.202)	0.281 (0.226)	0.450 (0.340)	0.445 (0.354)	0.415 (0.358)
				$\Delta\mathcal{M}_{obs}/\mathcal{M}_{obs}$			
6	20.744 (22.182)	9.828 (10.135)	3.308 (4.837)	1.480 (2.081)	1.268 (1.391)	1.276 (1.368)	1.131 (1.119)
8	21.574 (21.289)	0.613 (0.780)	0.917 (0.934)	0.822 (0.793)	0.780 (0.761)	0.763 (0.745)	0.748 (0.762)
10	20.421 (0.027)	0.164 (0.158)	0.640 (0.521)	0.691 (0.595)	0.682 (0.628)	0.666 (0.639)	0.644 (0.623)
12	0.016 (0.016)	0.109 (0.098)	0.263 (0.208)	0.551 (0.420)	0.609 (0.517)	0.597 (0.534)	0.579 (0.528)
14	0.011 (0.011)	0.080 (0.072)	0.150 (0.130)	0.428 (0.274)	0.547 (0.430)	0.545 (0.443)	0.476 (0.446)
16	0.008 (0.009)	0.064 (0.057)	0.114 (0.101)	0.267 (0.194)	0.485 (0.366)	0.479 (0.392)	0.450 (0.378)
18	0.208 (0.033)	0.056 (0.049)	0.098 (0.084)	0.179 (0.151)	0.432 (0.316)	0.424 (0.330)	0.379 (0.330)
				$\Delta d_L/d_L$			
6	2.340 (3.107)	1.792 (2.252)	1.503 (2.007)	1.259 (1.658)	1.061 (1.467)	1.119 (1.433)	1.252 (1.537)
8	3.197 (4.272)	2.847 (3.761)	2.465 (3.254)	2.017 (2.683)	1.631 (2.152)	1.693 (2.014)	1.909 (2.189)
10	3.869 (1.842)	1.226 (1.453)	2.090 (2.034)	1.989 (2.128)	1.717 (1.780)	1.691 (1.534)	1.740 (1.495)
12	1.144 (1.388)	0.926 (1.014)	1.019 (1.048)	1.330 (1.271)	1.338 (1.256)	1.272 (1.127)	1.263 (1.039)
14	0.988 (1.147)	0.785 (0.875)	0.750 (0.821)	0.995 (0.941)	1.083 (0.940)	1.006 (0.889)	0.926 (0.839)
16	0.878 (1.036)	0.688 (0.765)	0.656 (0.693)	0.747 (0.719)	0.924 (0.806)	0.852 (0.743)	0.803 (0.676)
18	2.011 (1.183)	0.609 (0.670)	0.609 (0.615)	0.619 (0.634)	0.795 (0.668)	0.750 (0.644)	0.657 (0.589)
				Δt_c (ms)			
6	189.9 (190.2)	185.6 (185.2)	142.4 (166.4)	58.8 (100.6)	54.6 (57.4)	65.2 (65.3)	71.4 (66.7)
8	191.5 (188.9)	11.0 (11.9)	17.3 (19.6)	19.2 (19.3)	26.8 (25.8)	36.7 (34.2)	44.6 (44.7)
10	188.8 (4.4)	7.0 (6.7)	11.1 (10.0)	14.9 (13.1)	21.3 (19.0)	26.1 (24.2)	32.3 (28.1)
12	3.6 (3.4)	6.0 (5.3)	8.2 (7.0)	11.8 (9.7)	18.0 (15.5)	22.3 (19.3)	24.7 (21.2)
14	3.1 (2.9)	5.1 (4.5)	6.7 (5.7)	9.4 (7.8)	15.0 (12.0)	19.1 (15.6)	19.7 (16.7)
16	2.9 (2.6)	4.5 (3.9)	5.8 (4.8)	7.6 (6.1)	13.1 (10.6)	15.8 (13.1)	17.6 (13.6)
18	9.0 (5.1)	4.0 (3.4)	5.1 (4.3)	6.5 (5.4)	11.9 (8.7)	13.6 (10.6)	14.4 (11.6)

[1] S. J. Waldman, The Advanced LIGO Gravitational Wave Detector, LIGO, 2011 (unpublished).

[2] J. Aasi *et al.* (LIGO Scientific Collaboration, Virgo Collaboration), arXiv:1304.0670.

[3] J. Aasi *et al.* (LIGO Scientific Collaboration), Class. Quantum Grav. **32**, 074001 (2015).

[4] F. Acernese *et al.* (VIRGO), Classical Quantum Gravity **32**, 024001 (2015).

[5] Y. Pan, A. Buonanno, M. Boyle, L. T. Buchman, L. E. Kidder, H. P. Pfeiffer, and M. A. Scheel, Phys. Rev. D **84**, 124052 (2011).

[6] J. Aasi, J. Abadie, B. P. Abbott, R. Abbott, T. D. Abbott, M. Abernathy, T. Accadia, F. Acernese *et al.* (LIGO Scientific Collaboration, Virgo Collaboration), arXiv:1304.0670.

[7] P. Ade *et al.* (Planck), Astron. Astrophys. **571**, A16 (2014).

[8] A. Buonanno, Y. Chen, and T. Damour, Phys. Rev. D **74**, 104005 (2006).

[9] P. Ajith, M. Hannam, S. Husa, Y. Chen, B. Bruegmann *et al.*, Phys. Rev. Lett. **106**, 241101 (2011).

[10] K. Belczynski, A. Buonanno, M. Cantiello, C. L. Fryer, D. E. Holz, I. Mandel, M. C. Miller, and M. Walczak, Astrophys. J. **789**, 120 (2014).

[11] P. Amaro-Seoane, J. R. Gair, M. Freitag, M. C. Miller, I. Mandel, C. J. Cutler, and S. Babak, Classical Quantum Gravity **24**, R113 (2007).

[12] J. R. Gair, I. Mandel, M. C. Miller, and M. Volonteri, Gen. Relativ. Gravit. **43**, 485 (2011).

[13] I. Mandel, J. R. Gair, and M. C. Miller, in *Twelfth Marcel Grossmann Meeting on General Relativity*, edited by T. Damour, R. T. Jantzen, and R. Ruffini (World Scientific, Paris, 2012), p. 1676.

[14] M. Volonteri, Science **337**, 544 (2012).

[15] R. Fender and T. Belloni, Science **337**, 540 (2012).

[16] M. Bachetti, F. Harrison, D. Walton, B. Grefenstette, D. Chakrabarty *et al.*, Nature (London) **514**, 202 (2014).

[17] C. Motch, M. Pakull, R. Soria, F. Gris, and G. Pietrzyski, Nature (London) **514**, 198 (2014).

[18] J. Liu, J. N. Bregman, Y. Bai, S. Justham, and P. Crowther, Nature (London) **503**, 500 (2013).

[19] D. R. Pasham, T. E. Strohmayer, and R. F. Mushotzky, Nature (London) **513**, 74 (2014).

[20] M. Volonteri, AIP Conf. Proc. **1480**, 289 (2012).

[21] A. Sesana, J. Gair, I. Mandel, and A. Vecchio, Astrophys. J. Lett. **698**, L129 (2009).

[22] P. Amaro-Seoane and L. Santamaria, Astrophys. J. **722**, 1197 (2010).

[23] G. D. Quinlan and S. L. Shapiro, Astrophys. J. **343**, 725 (1989).

[24] A. Buonanno and B. Sathyaprakash, arXiv:1410.7832.

[25] P. Peters, Phys. Rev. **136**, B1224 (1964).

[26] L. Wen, Astrophys. J. **598**, 419 (2003).

[27] L. Blanchet, Living Rev. Relativity **9**, 4 (2006).

[28] R. W. Hellings and T. A. Moore, Classical Quantum Gravity **20**, S181 (2003).

[29] C. Van Den Broeck and A. S. Sengupta, Classical Quantum Gravity **24**, 1089 (2007).

[30] P. Ajith and S. Bose, Phys. Rev. D **79**, 084032 (2009).

[31] S. Bose, S. Ghosh, and P. Ajith, Classical Quantum Gravity **27**, 114001 (2010).

[32] T. B. Littenberg, J. G. Baker, A. Buonanno, and B. J. Kelly, Phys. Rev. D **87**, 104003 (2013).

[33] H.-S. Cho, E. Ochsner, R. O'Shaughnessy, C. Kim, and C.-H. Lee, Phys. Rev. D **87**, 024004 (2013).

[34] R. O'Shaughnessy, B. Farr, E. Ochsner, H.-S. Cho, C. Kim, and C.-H. Lee, Phys. Rev. D **89**, 064048 (2014).

[35] R. O'Shaughnessy, B. Farr, E. Ochsner, H.-S. Cho, V. Raymond, C. Kim, and C.-H. Lee, Phys. Rev. D **89**, 102005 (2014).

[36] L. Pekowsky, J. Healy, D. Shoemaker, and P. Laguna, Phys. Rev. D **87**, 084008 (2013).

[37] V. Varma, P. Ajith, S. Husa, J. C. Bustillo, M. Hannam, and M. Pürrer, Phys. Rev. D **90**, 124004 (2014).

[38] J. Calderón Bustillo, A. Bohé, S. Husa, A. M. Sintes, M. Hannam, and M. Pürrer, Phys. Rev. D **92**, DB11508 (2015).

[39] E. Berti, V. Cardoso, J. A. Gonzalez, U. Sperhake, M. Hannam, S. Husa, and B. Brügmann, Phys. Rev. D **76**, 064034 (2007).

[40] E. Berti, J. Cardoso, V. Cardoso, and M. Cavaglià, Phys. Rev. D **76**, 104044 (2007).

[41] S. Hadar, B. Kol, E. Berti, and V. Cardoso, Phys. Rev. D **84**, 047501 (2011).

[42] I. Kamaretsos, M. Hannam, S. Husa, and B. Sathyaprakash, Phys. Rev. D **85**, 024018 (2012).

[43] I. Kamaretsos, M. Hannam, and B. Sathyaprakash, Phys. Rev. Lett. **109**, 141102 (2012).

[44] L. London, D. Shoemaker, and J. Healy, Phys. Rev. D **90**, 124032 (2014).

[45] S. Gossan, J. Veitch, and B. Sathyaprakash, Phys. Rev. D **85**, 124056 (2012).

[46] J. Meidam, M. Agathos, C. Van Den Broeck, J. Veitch, and B. Sathyaprakash, Phys. Rev. D **90**, 064009 (2014).

[47] C. Capano, Y. Pan, and A. Buonanno, Phys. Rev. D **89**, 102003 (2014).

[48] A. Buonanno and T. Damour, Phys. Rev. D **59**, 084006 (1999).

[49] A. Buonanno and T. Damour, Phys. Rev. D **62**, 064015 (2000).

[50] LSC Algorithm Library Suite, http://www.lsc-group.phys.uwm.edu/lal.

[51] T. Damour, A. Nagar, and S. Bernuzzi, Phys. Rev. D **87**, 084035 (2013).

[52] L. T. Buchman, H. P. Pfeiffer, M. A. Scheel, and B. Szilagyi, Phys. Rev. D **86**, 084033 (2012).

[53] Y. Pan, A. Buonanno, A. Taracchini, M. Boyle, L. E. Kidder, A. H. Mroué, H. P. Pfeiffer, M. A. Scheel, B. Szilágyi, and A. Zenginoglu, , Phys. Rev. D **89**, 061501 (2014).

[54] I. Hinder, A. Buonanno, M. Boyle, Z. B. Etienne, J. Healy *et al.*, Classical Quantum Gravity **31**, 025012 (2014).

[55] B. Szilagyi, J. Blackman, A. Buonanno, A. Taracchini, H. P. Pfeiffer *et al.*, Phys. Rev. Lett. **114**, LB15222 (2015).

[56] J. Skilling, Bayesian Analysis **1**, 833 (2006).

[57] F. Feroz and M. P. Hobson, Mon. Not. R. Astrons. Soc. **384**, 449 (2008).

[58] F. Feroz, M. P. Hobson, and M. Bridges, Mon. Not. R. Astron. Soc. **398**, 1601 (2009).

[59] F. Feroz, M. P. Hobson, E. Cameron, and A. N. Pettitt, arXiv:1306.2144.

[60] P. Graff, F. Feroz, M. P. Hobson, and A. Lasenby, Mon. Not. R. Astron. Soc. **421**, 169 (2012).

[61] J. Veitch *et al.*, Phys. Rev. D **91**, 042003 (2015).

[62] W. G. Anderson, P. R. Brady, J. D. Creighton, and É. É. Flanagan, Phys. Rev. D **63**, 042003 (2001).

[63] J. Abadie *et al.*, Phys. Rev. D **85**, 082002 (2012).

[64] J. Aasi, J. Abadie, B. P. Abbott, R. Abbott, T. D. Abbott, M. Abernathy, T. Accadia, F. Acernese, C. Adams, T. Adams *et al.*, Phys. Rev. D **87**, 022002 (2013).

[65] B. Sathyaprakash and S. Dhurandhar, Phys. Rev. D **44**, 3819 (1991).

[66] R. Balasubramanian, B. S. Sathyaprakash, and S. V. Dhurandhar, Phys. Rev. D **53**, 3033 (1996).

[67] B. J. Owen, Phys. Rev. D **53**, 6749 (1996).

[68] J. Abadie *et al.* (LIGO Scientific Collaboration and Virgo Collaboration), Phys. Rev. D **83**, 122005 (2011).

[69] N. J. Cornish and T. B. Littenberg, Classical Quantum Gravity **32**, 135012 (2015).

[70] T. B. Littenberg and N. J. Cornish, Phys. Rev. D **91**, 084034 (2015).

[71] T. Futamase and Y. Itoh, Living Rev. Relativity **10**, 2 (2007).

[72] E. Berti, V. Cardoso, and C. M. Will, Phys. Rev. D **73**, 064030 (2006).

[73] M. Pürrer, Classical Quantum Gravity **31**, 195010 (2014).

[74] S. Marsat (private communication).

[75] J. Veitch, M. Pürrer, and I. Mandel, Phys. Rev. Lett. **114**, LC15628 (2015).

[76] A. Taracchini, A. Buonanno, Y. Pan, T. Hinderer, M. Boyle, D. A. Hemberger, L. E. Kidder, G. Lovelace, A. H. Mroué, H. P. Pfeiffer, M. A. Scheel, B. Szilágyi, N. W. Taylor, and A. Zenginoglu, Phys. Rev. D **89**, 061502 (2014).